The Astrophysical Journal, 940:95 (21pp), 2022 November 20 https://doi.org/10.3847/1538-4357/ac8b85

The Early Solar System Abundance of Iron-60: New Constraints from Chondritic Silicates

János Kodolányi[1], Peter Hoppe[1], Christian Vollmer[2], Jasper Berndt[2], and Maren Müller[3]
[1] Max Planck Institute for Chemistry, Hahn-Meitner-Weg 1, D-55128 Mainz, Germany; janos.kodolanyi@gmail.com
[2] Westfälische Wilhelms-Universität Münster, Institut für Mineralogie,, Corrensstraße 24, D-48149 Münster, Germany
[3] Max Planck Institute for Polymer Research, Ackermannweg 10, D-55128 Mainz, Germany
Received 2022 May 31; revised 2022 August 14; accepted 2022 August 19; published 2022 November 23

Abstract

The abundance of iron-60 in the early solar system is important for planetary evolution models, and has been hotly debated. To put further constraints on the initial $^{60}Fe/^{56}Fe$ ratio of the solar system, here we present new iron-nickel isotope data, measured in situ by NanoSIMS, for 14 silicate chondrules from three carbonaceous and three unequilibrated ordinary chondrites. NanoSIMS measurements were performed at high spatial resolution (200–300 nm primary beam diameter), to avoid inclusion of unwanted phases in the analysis volume. The average initial $^{60}Fe/^{56}Fe$ ratios that can be estimated from our pooled chondrule data are 2.1 ($\pm$1.3) $\times 10^{-7}$ and 0.8 ($\pm$1.0) $\times 10^{-7}$ for carbonaceous and ordinary chondrites, respectively (1σ uncertainties). The estimated average initial $^{60}Fe/^{56}Fe$ ratio of all analyzed chondrules is 1.0 ($\pm$0.7) $\times 10^{-7}$. These results are inconsistent with initial $^{60}Fe/^{56}Fe$ ratios $>2.4 \times 10^{-7}$ (2σ upper limit of our entire data set) reported in the literature for some chondrule silicates based on in situ isotope data, and agree better with our previously published in situ data on chondritic troilites ($0.10 \pm 0.15 \times 10^{-7}$), as well as with $^{60}Fe/^{56}Fe$ ratios estimated from isotope data of bulk meteorites and chondrules ($0.10–0.75 \times 10^{-7}$). Our isotope data hint at a possible difference between the initial $^{60}Fe/^{56}Fe$ ratios of the early solar system's two major isotope reservoirs, with the carbonaceous chondritic reservoir having higher iron-60 abundance than the non-carbonaceous reservoir. Nevertheless, in light of similar *hints* in the literature, this possibility deserves further investigation.

Unified Astronomy Thesaurus concepts: Isotopic abundances (867); Solar system (1528)

1. Introduction

The abundance of the short-lived radioactive isotope iron-60 (half-life: 2.62 ± 0.04 Myr; Rugel et al. 2009 throughout this paper, quoted uncertainties represent 68% confidence intervals, abbreviated as $\pm 1\sigma$, unless stated otherwise) is an important parameter for models of early solar system planetary evolution. This is because the heat produced by the decay of iron-60 and that of its immediate decay product cobalt-60 (2.712 MeV in total per ^{60}Fe; Castillo-Rogez et al. 2009) may have played a role in the melting of metal in the cores of some of the early planetesimals, such as the IVB iron meteorite parent body (Neumann et al. 2018). In the small (diameter $<\sim$100 km) sulfide-poor parent body of IVB irons, metal melting in the core may have occurred as late as 3 or more million years after solar system formation (Neumann et al. 2018; Spitzer et al. 2021). Such a late metal melting requires a heat source in addition to aluminum-26 (half-life: 705 ± 24 kyr; Norris et al. 1983), the main heat source of melting in the earliest formed planets (Moskovitz & Gaidos 2011; Neumann et al. 2018). Iron-60 may have been this additional heat source, provided it was present in sufficient concentration.

The initial $^{60}Fe/^{56}Fe$ ratio of the solar system, i.e., the $^{60}Fe/^{56}Fe$ ratio at the time the so-called canonical calcium-aluminum-rich inclusions (CCAIs; Jacobsen et al. 2008) formed, $^{60}Fe/^{56}Fe_{CCAI}$, has been the subject of numerous studies. The most widely used estimates, 1.15 ($\pm$0.13) $\times 10^{-8}$ and 1.01 ($\pm$0.14) $\times 10^{-8}$, are those of Tang & Dauphas (2012, 2015, respectively). They were largely calculated from bulk rock and bulk mineral isochrons of quenched angrites and basaltic eucrites, based on precise nickel isotope measurements by MC-ICP-MS (multi-collector inductively coupled plasma mass spectrometry). In the absence of aqueous alteration or thermal metamorphism, these rocks provide currently the best fossil records of iron-60 in the early solar system: They tapped iron and nickel isotopically (presumably) homogenized magmas, cooled down sufficiently fast to prevent significant iron-nickel redistribution or isotopic re-equilibration upon cooling, and they are old enough (formation 3–5 Myr after CCAIs; Schiller et al. 2010; McKibbin et al. 2015; Hublet et al. 2017) to have had live iron-60 at their formation.

The $^{60}Fe/^{56}Fe_{CCAI}$ ratio estimated from the compositions of angrites and eucrites may not be representative of the entire solar system, however. Based on their isotope composition, meteorites can be divided into *carbonaceous* (CC) and *non-carbonaceous* (NC) groups (Warren 2011). The members of each group define distinct arrays in the stable chromium-nickel-titanium-oxygen isotope space, but their isotopic differences extend to a number of other elements as well, including iron (Liszewska et al. 2021). The CC–NC isotopic dichotomy is thought to at least partially reflect spatial isotopic heterogeneity in the early solar system, with CC meteorites sampling the outer, NC meteorites in the inner solar system (e.g., Kruijer et al. 2017). Angrites and eucrites belong to the CC NC group of meteorites, but precise isochrons are not available for meteorites from the CC group. Nevertheless, IVB and IID iron meteorites, which are pieces of the once-molten cores of small planetesimals and belong to the CC isotopic reservoir, have sub-chondritic Fe/Ni ratios ($\sim$5 and $\sim$9, respectively), and they are depleted in nickel-60 relative to many CC chondrites

and most NC meteorites (Steele et al. 2011; Nanne et al. 2019; Cook et al. 2021). Steele et al. (2012) and Cook et al. (2021) used this fact to calculate initial $^{60}Fe/^{56}Fe$ ratios for the IVB ($0.75\ (\pm0.33) \times 10^{-7}$ and $2.7\ (\pm0.55) \times 10^{-7}$, respectively) and IID meteorites ($3.5\ (\pm0.75) \times 10^{-7}$; Cook et al. 2021). These initial $^{60}Fe/^{56}Fe$ ratios vary considerably because of the difference between the reference nickel isotope compositions used to calculate the nickel-60 "deficit" (CO and CV chondrites versus CI chondrites in the Steele et al. 2012, and Cook et al. 2021 studies, respectively), and because of the difference in the presumed timing of Fe/Ni fractionation in the iron meteorites and their precursors relative to the formation of CCAIs. (Steele et al. 2012 assumed that Fe/Ni fractionation happened instantaneously after CCAI formation, whereas Cook et al. (2021) assumed that several million years had passed between the formation of CCAIs and Fe/Ni fractionation in the IVB and IID parent bodies.) Regardless, these initial $^{60}Fe/^{56}Fe$ ratios are much higher than even the $^{60}Fe/^{56}Fe_{CCAI}$ ratio based on angrite and basaltic eucrite data. This may be a hint that the CC isotope reservoir had a higher $^{60}Fe/^{56}Fe_{CCAI}$ ratio than the NC reservoir. However, because of the similarity between the non-mass-dependent nickel isotope anomalies of IVB and IID meteorites and those of some CM and CV chondrites (also CC reservoir), which have about chondritic Fe/Ni ratios (~18; Steele et al. 2011, 2012; Nanne et al. 2019), the interpretation of the nickel-60 "deficit" observed in IVB and IID meteorites in terms of the evolution of radiogenic nickel-60 in chondritic matter remains uncertain.

In contrast to the majority of isotope data from bulk samples, a large number of isotope data measured in situ in chondritic silicates and troilites, using SIMS (secondary ion mass spectrometry) or NanoSIMS (a secondary ion mass spectrometer capable of submicron spatial resolution), suggested that the solar system's initial $^{60}Fe/^{56}Fe$ ratio might have been 1–2 orders of magnitude higher, up to 10^{-6} (Mostefaoui et al. 2005; Mishra & Goswami 2014; Mishra et al. 2016; Telus et al. 2018). 90% of these in situ analyses were performed on minerals in unequilibrated ordinary chondrites (UOCs), so they should be more representative of the iron-60 abundance in the NC than in the CC isotope reservoir. Recent in situ measurements of a chondrule from the Semarkona UOC using resonance ionization mass spectrometry (Trappitsch et al. 2018) and of troilites from Semarkona and two carbonaceous chondrites (Dominion Range 08006 and Allan Hills A77307) using NanoSIMS (Kodolányi et al. 2022) were consistent with the low iron-60 abundance ($^{60}Fe/^{56}Fe_{CCAI} \sim 10^{-8}$, see above) calculated by Tang & Dauphas (2012, 2015) based on data from bulk samples. Common in all of the isotope data sets obtained in situ is that the measured isotope compositions do not define precise, true isochrons, even in individual chondrules.

The range of estimated $^{60}Fe/^{56}Fe_{CCAI}$ ratios and the difference between estimates based on bulk mineral/rock and in situ mineral isotope data require explanation. When it comes to differences in $^{60}Fe/^{56}Fe_{CCAI}$ ratios, age variations among samples are irrelevant, but the measurements themselves or the calculation procedure of $^{60}Fe/^{56}Fe_{CCAI}$ ratios may introduce bias. For example, inclusion of an iron-rich vein in an analysis, that formed after all the iron-60 of its host, the actual target, had already decayed can shift Fe/Ni ratios upward, while having no significant effect on the sample's nickel isotope composition (e.g., Telus et al. 2016). The initial $^{60}Fe/^{56}Fe$ ratio calculated from such analyses will be an underestimation of the true initial $^{60}Fe/^{56}Fe$ ratio. Similarly, iron loss from a target due, e.g., to thermal metamorphism, can decrease its Fe/Ni ratio, while leaving its nickel isotope compositions unaffected. The initial $^{60}Fe/^{56}Fe$ ratio calculated from such data would be an overestimation of the true value. By improving the spatial control of in situ measurements, or the procedure of mineral separation for bulk analyses, the chance that the above bias occurs can be drastically reduced.

Here, we provide additional constraints on the solar system's initial $^{60}Fe/^{56}Fe$ ratio, based on the nickel isotope compositions and Fe/Ni ratios of chondritic silicates. Our goal was to address the issues detailed above. First, we studied primitive chondrites from both the NC and CC isotopic groups, to see if further analysis of CC chondrites could provide some clues to the potential difference between the initial $^{60}Fe/^{56}Fe$ ratios of the two large isotope reservoirs (if there was any, see above). Second, we collected our isotope data in situ, at submicron spatial resolution, using NanoSIMS, and utilized the instrument's imaging mode. This allowed us to have the best possible control over what is included in our analyses. Third, using transmission electron microscopy, we investigated electron-transparent slices of some of the silicate minerals after NanoSIMS measurements, to check for the presence of veins and inclusions too small to be picked up by NanoSIMS ion imaging, and to see if there was any evidence for the disturbance of the iron-nickel system that could have affected the elemental or isotopic compositions since the formation of the target minerals.

In addition, we dated some of the studied chondrules using the aluminum–magnesium isotope system, relative to anchors of known absolute age. Our goal with the relative dating was to gather information about the age range of the studied chondrules, which, in combination with nickel isotope data, could allow us to constrain the initial $^{60}Fe/^{56}Fe$ ratio of the solar system.

2. Samples

We selected six low petrologic type (2–3) chondrites for our study (Queen Alexandra Range 97008, Meteorite Hills 00526, Northwest Africa 8276, Dominion Range 08006, Allan Hills A77307, and Meteorite Hills 00426; Table 1). Low petrologic type meteorites were chosen because they have almost no signs of thermal re-equilibration that could have overprinted the original isotopic and elemental compositions of chondrule forming silicates. Although most of the studied meteorites show some minor signs of aqueous alteration, these are observed in the fine-grained matrix (e.g., growth of phyllosilicates) and/or veins, and all of our meteorites have silicate chondrules and chondrule fragments that are free of any evidence of water-rock interaction. The primary targets of iron-nickel isotope analyses were such chondrules and chondrule fragments. We define chondrule fragments as angular clasts with irregular shapes that have mineral assemblages and textures resembling those seen in chondrules. We will refer to chondrule fragments as chondrules hereafter. The isotope analysis of chondrules was preferred because the conditions and timing of chondrule mineral formation have been constrained fairly well by previous studies (see Section 5.6.).

Ideally, our targets would have Fe/Ni ratios of several thousand or more. However, it was not always possible to identify phases or areas of minerals with such Fe/Ni ratios

Table 1
Meteorites and Their Chondrules Analyzed for the Present Study

Sample	Abbreviation Used in the Text	Group	Petrologic Type	Chondrule	Longest Diameter [μm]	Chondrule Texture[a]	Average Mg# of Mafic Phase(s)[b]	±	Maximum Fe/Ni[c]	±	Remark[d]
CC meteorites											
Dominion Range 08006	DOM 08006	CO	3	b46	250	GO/BO	53.8	0.4	11,090	576	
				b47	240	PO	58.6	0.3	869	7	
				b49	170	GO	42.1	0.9	62,355	3650	
Allan Hills 77307	ALHA77307	CO	3.0	b13	400	PO	65.2	4.0	1343	27	
				b16	260	GO	32.2	0.2	3924	162	(1)
Meteorite Hills 00426	MET 00426	CR	2	b1	600	PO	67.5	1.7	800	11	
				b4	140	PO	72.6	1.2	713	9	
NC meteorites											
Meteorite Hills 00526	MET 00526	L(LL)	3.05	b1	2250	POP	84.3	0.3	12,358	286	(2)
Queen Alexandra Range 97008	QUE 97008	L	3.05	b9	1100	C	70.6	0.7	52,913	1881	
				b15	1100	POP	84.1	0.3	12,549	284	
				b16	2600	POP	83.7	0.2	8605	193	
Northwest Africa 8276	NWA 8276	L	3.00	b1	1000	POP	71.6	0.2	6667	106	
				b15	1400	BO/RP	81.1	1.7	25,080	984	
				b20	1000	POP	75.9	0.1	22,581	1159	

Notes. Meteorite groups and types according to Meteoritical Bulletin Database (2022 May).

[a] GO = granular olivine, BO = barred olivine, PO = porphyritic olivine, POP = porphyritic olivine-pyroxene, C = cryptocrystalline, RP = radial pyroxene.

[b] Mg# = $100 \times \mathrm{Mg}/(\mathrm{Mg+Fe+Mn+Ni})_{\mathrm{atomic}}$. Average Mg# of mafic phases that were analyzed by NanoSIMS for their nickel isotope composition and Fe/Ni ratios. Mg#-s were calculated from EPMA or SEM-EDX data.

[c] From NanoSIMS data.

[d] (1) All EDX point analyses of olivine are influenced by the mesostasis as a result of small olivine grain size (smallest diameter <2 μm) and (presumably) the presence of melt inclusions in olivine; the Mg# quoted here was calculated from the analysis with the least amount of mesostasis addition (Si cation number based on 4 O: Si = 0.9958). (2) Quoted Mg# is for calcium-rich pyroxene; Mg# of olivine is 85.00 ± 0.28.

Table 2
NanoSIMS Measurement Conditions

Measurements	Al-Mg	Fe–Ni
Primary ions	$^{16}O^-$	$^{16}O^-$
Primary beam intensity	12–13 pA	∼75 or ∼500 pA
Primary beam diameter	∼150 nm	200–300 nm
Measurement mode	Spot or imaging	Imaging
Analyzed area/spot[a]	6×6 μm^2	3×3 μm^2 or 6×6 μm^2
Measurement duration/spot	55 minutes	55 or 109 minutes
Analyzed isotopes	^{24}Mg, ^{25}Mg, ^{26}Mg, ^{27}Al, ^{29}Si	^{29}Si, $^{46}Ti+^{46}Ca$, ^{54}Fe, ^{60}Ni, ^{62}Ni
Minimum count rate on ^{62}Ni		0.2 cps (olivine), 2 cps (pyroxene)
Maximum dynamic background correction on ^{60}Ni		3%
Maximum dynamic background correction on ^{62}Ni		2.2%
Internal standardization	Yes, based on $^{25}Mg/^{24}Mg$	No
External standardization	San Carlos olivine ($^{25}Mg/^{24}Mg$ ratios), NIST SRM 611 (Al/Mg ratios)	Terrestrial enstatite (pyroxenes[b]), San Carlos olivine (olivine)

Notes.
[a] Signal from pit edges was disregarded during data reduction.
[b] Terrestrial enstatite was also used for external standardization of the Fe–Ni isotope measurements of the "b9" cryptocrystalline chondrule in QUE 97008.

prior to the NanoSIMS analyses. Furthermore, the mafic phases of some of the analyzed chondrules had variable Fe/Ni ratios (see below), so even if electron microprobe data indicated less than ideal Fe/Ni ratios, we often still saw it feasible to carry out NanoSIMS iron-nickel isotope analysis. In practice, all mafic silicates with FeO_{total} contents (iron oxide contents with all iron assumed to be above ∼10 wt.% (weight percent) were considered potential targets for iron-nickel isotope analysis. Such "iron-rich" silicates were preferred because for the same Fe/Ni ratio, a silicate with a higher iron content will provide better counting statistics on nickel than one that is poor in iron (we have not observed a correlation between iron contents and Fe/Ni ratios). For aluminum–magnesium dating, we chose chondrules with at least one phase (in most cases anorthite) that had Al/Mg ratios of ∼40 or more, besides magnesium-rich enstatite or olivine.

3. Analytical Methods

3.1. Scanning Electron Microscopy and Electron Probe Microanalysis

Backscattered electron (BSE) images and energy-dispersive X-ray (EDX) element maps together with point analysis (EDX or electron probe microanalysis) on conventional petrographic thin sections of the studied meteorites were used to identify spots within chondrules that were likely suitable for later isotope analysis with NanoSIMS. BSE imaging and EDX element mapping were carried out with the LEO 1530 field emission scanning electron microscope (SEM) at the Max Planck Institute for Chemistry (Mainz, Germany), which is equipped with an Oxford X-Max 80 mm^2 EDX detector. The same instrument was used for EDX point analysis as well. Analytical conditions of the EDX point analysis were 15 kV acceleration voltage, and 90 s measurement time (without detector dead-time). We used AZtec versions 2.4 and 3.1 for visualization and quantification of EDX data. We also quantitatively measured the nickel content of some of the silicate phases, using the JEOL JXA 8530F electron microprobe at the Westfälische Wilhelms-University of Münster (Münster, Germany). For these measurements, the acceleration voltage was 15 kV and the beam current was 50 or 80 nA. The higher beam current (in combination with longer counting times) was used to decrease the detection limit for nickel (from 200 to 30 parts per million by weight). The probe diameter was about 2 μm. Raw data were processed following the PRZ method (Phi-Rho-Z, a ZAF correction that uses a Gaussian depth distribution function for the calculation of absorption correction; Armstrong 1991) to correct for matrix effects. Quantification was based on a WDS-intensity comparison of unknowns with natural and synthetic silicate and oxide reference materials. Analyzing the same material with EPMA and SEM-EDX allowed us to have a direct comparison of major and minor element compositional data from the two analysis methods. Figure A1 (Appendix) shows such comparisons for major and minor elements, and demonstrates excellent reproducibility across the methods.

3.2. Isotope Analysis

Isotope measurements were performed using the NanoSIMS 50 of the Max Planck Institute for Chemistry in Mainz, Germany, using the Hyperion primary ion source in O^- mode. The most important analytical parameters of iron-nickel and aluminum–magnesium isotope analyses are listed in Table 2. Typical pits of NanoSIMS measurements are shown in Figures 1(a)–(c).

3.2.1. Magnesium-aluminum Analysis

Sample and standard measurement conditions were the same in the case of the aluminum–magnesium isotope measurements, with each analysis of the San Carlos olivine (used as a magnesium isotope standard; Table 2) split in two for standard-sample bracketing. There was no standard-sample bracketing during the measurements of the NIST 611 (National Institute of Standards and Technology 611) Standard Reference Material used to obtain the Al/Mg sensitivity ratio (Table 2).

Correction of the quasi-simultaneous arrival (QSA) effect (Slodzian et al. 2004) during aluminum–magnesium isotope analysis was essential because the external magnesium isotope

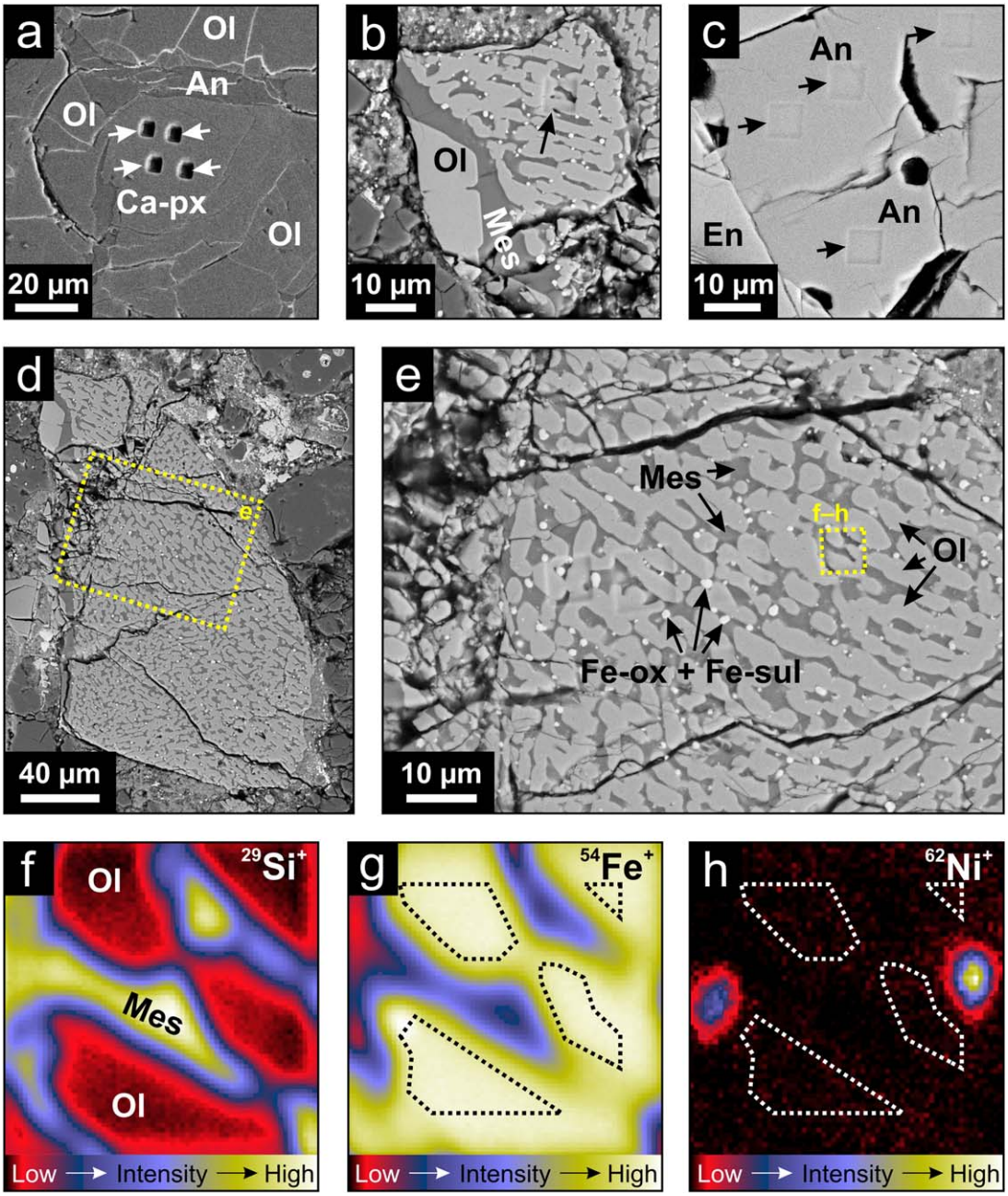

Figure 1. (a)–(c) SEM-BSE images of typical NanoSIMS analysis pits. (a) Iron-nickel analysis pits (white arrows) with 3×3 μm^2 nominal size formed by ~500 pA O^- primary beam (MET 00526, chondrule b1). (b) Iron-nickel analysis pits (black arrow) with 6×6 μm^2 nominal size formed by ~75 pA O^- primary beam (DOM 08006, chondrule b49). (c) Aluminum–magnesium analysis pits (black arrows) with 6×6 μm^2 nominal size formed by ~12 pA O^- primary beam (QUE 97008, chondrule b15). (d) and (e) BSE images of chondrule b49 from DOM 08006. (f)–(h) Ion images from the area indicated in (e). Each ion image is 6×6 μm^2. Dotted lines in (g) and (h) indicate the area of signal integration for quantification of isotope measurements. Abbreviations: Ol = olivine, An = anorthite, En = enstatite, Ca-px = calcium-rich pyroxene, Mes = mesostasis, Fe-ox = iron oxide, Fe-sul = iron sulfide.

reference (San Carlos olivine) was magnesium-rich (MgO: 49.5 wt.%; De Hoog et al. 2010), whereas the high Al/Mg chondrule phases were magnesium-poor (MgO: <1 wt.%). Without QSA correction, $^{25}Mg/^{24}Mg$ and $^{26}Mg/^{24}Mg$ ratios measured in the magnesium-rich reference are higher than in the magnesium-poor high Al/Mg phase, even if the two phases have the same $^{25}Mg/^{24}Mg$ and $^{26}Mg/^{24}Mg$ ratios (i.e., even if there was no radiogenic growth of magnesium-26 from the decay of aluminum-26 in the high Al/Mg phase). Thus, magnesium-26 excesses in the magnesium-poor phase are overestimated without the QSA correction of the reference. A generalized formula for the correction of the QSA effect was provided by Hoppe et al. (2013):

$$R_{\text{true}} = \frac{R_{\text{meas}}}{(1 + a \times K)},$$

where R_{true} and R_{meas} are the true and measured isotope ratios (with the more abundant isotope being the denominator), respectively, K is the ratio of the secondary ions to the primary ions of the more abundant isotope, and a is an element- and matrix-specific scaling factor. For the current study, the a factor was estimated to be 2.5 ± 0.5 from the analysis of three pyroxenes in NWA 8276, and it was verified by analyzing

meteorite matrices as unknowns (assumed terrestrial magnesium isotope composition). Uncertainties of reported magnesium isotope ratios and calculated initial $^{26}Al/^{27}Al$ ratios include the uncertainty of a (Section 4).

3.2.2. Iron-nickel Analysis

In the case of iron-nickel isotope measurements, we used the NanoSIMS "image mode", which allowed irregular areas within single measurement fields to be defined for signal integration. These areas were tailored to cover specific phases, to cover areas that were Ti- and/or Ca-poor (the rationale behind the latter is explained below), or to avoid veins and inclusions. Figures 1(d)–(h) show how the excellent spatial control of analysis, provided by the combination of the submicron primary beam diameter (200–300 nm; Table 2) and the image mode enables the analysis of specific phases in chondrules with complex, micron-scale structure. In the example, rounded olivine crystals with 1–2 μm width and 2–10 μm length occur together with glassy silicate-dominated mesostasis and compound submicron iron-oxide + iron-sulfide grains (see Section 4 for more details of the mineralogy of this chondrule). The latter are nickel-rich (Fe/Ni $\approx$ 220), and would dominate nickel isotope compositions with their presumably terrestrial nickel isotope composition, if included in the analyzed volume. The olivines have high Fe/Ni ratios (33,000 in the current example, but up to 62,000 in the chondrule, see Section 4), so they could have a small nickel-60 surplus from in situ iron-60 decay. They were therefore of interest for nickel isotope analysis. In imaging mode, and with the low-diameter primary ion beam, the analysis of the olivines was possible without the diluting effects of the compound iron-oxide + iron-sulfide grains.

Samples and standards were analyzed using the same analytical conditions, but standard measurements were split in two, providing standard-sample bracketing. The standards used as nickel isotope references (San Carlos olivine and terrestrial enstatite, both with assumed terrestrial nickel isotope composition; Table 2) were also used to determine Fe/Ni sensitivity ratios. The Fe/Ni sensitivity ratios determined for olivine (1.3–1.6 during the course of our measurements) were usually a bit higher than those determined for enstatite (1.3–1.4). When analyzed during the same analytical session, the two standards yielded identical nickel isotope ratios within analytical uncertainty.

Although the mass resolution of our measurements was sufficient to separate iron and nickel isotope peaks from hydride interference peaks ($M/\Delta M > 4000$; Cameca definition, see Hoppe et al. 2013), this resolution is insufficient to allow the ^{46}Ca and ^{46}Ti peaks to be distinguished from each other. These species were measured along with iron and nickel isotopes to monitor the potential contribution of the tail of the $^{46}Ti^{16}O$+$^{46}Ca^{16}O$ peak to ^{62}Ni.

The dynamic background during iron-nickel isotope analyses was estimated from measurements with the detectors' deflection plate voltages −12V off-peak, i.e., the same way as estimated by Mostefaoui et al. (2005) and Kodolányi et al. (2022). This detuning corresponds to about −28 mamu (mamu = milli atomic mass unit) at masses 60–62.

Another similarity to our troilite measurements (Kodolányi et al. 2022) is that we measured the nickel isotopes −0.5 V off center, to minimize the effect of the tails of the $^{59}Co^{1}H$ and $^{46}Ti^{16}O$ + $^{46}Ca^{16}O$ isobars on ^{60}Ni and ^{62}Ni, respectively. We note however, that according to our EPMA data (see Section 4), the analyzed chondrule silicates have lower cobalt concentrations than the most nickel-poor troilites (about half as much, or even less), whereas their nickel contents are higher than the nickel contents of the same troilites (here the difference can be orders of magnitude), so the $^{59}Co^{1}H$ interference, which was shown to be negligible for troilites (Kodolányi et al. 2022), should have even less potential to affect our silicate measurements. The effect of the tails of the $^{46}Ti^{16}O$ and $^{46}Ca^{16}O$ isobars on ^{62}Ni must also be small or nonexistent, as there is a slight positive correlation between $^{60}Ni/^{62}Ni$ and $(^{46}Ti+^{46}Ca)/^{62}Ni$ ratios of pooled data from all studied chondrites (correlation coefficient: 0.12, slope: $3.85 \pm 4.14 \times 10^{-5}$; linear regression following Mahon 1996, and assuming that the uncertainties of the two ratios are uncorrelated). A negative correlation between $^{60}Ni/^{62}Ni$ and $(^{46}Ti+^{46}Ca)/^{62}Ni$ ratios would be a strong indication of $^{46}Ti^{16}O$ and $^{46}Ca^{16}O$ interference on nickel-62. However, the effect of $^{46}Ti^{16}O$ and $^{46}Ca^{16}O$ interferences is difficult to establish if (Ti+Ca)/Ni and Fe/Ni ratios are both primarily the result of variations in the nickel content of the analyzed minerals and there is a positive correlation between $^{60}Ni/^{62}Ni$ and Fe/Ni ratios (as expected in case of in situ iron-60 decay) because in this case a positive correlation is expected between $^{60}Ni/^{62}Ni$ and $(^{46}Ti+^{46}Ca)/^{62}Ni$ ratios, which is what we observe, as weak as it may be. Since the exact correlation between $^{60}Ni/^{62}Ni$ and $(^{46}Ti+^{46}Ca)/^{62}Ni$ ratios is not known a priori, it is possible that an observed small positive correlation between $^{60}Ni/^{62}Ni$ and $(^{46}Ti+^{46}Ca)/^{62}Ni$ ratios resulted from the superposition of a stronger true correlation between $^{60}Ni/^{62}Ni$ and $(^{46}Ti+^{46}Ca)/^{62}Ni$ ratios and a small decrease of $^{60}Ni/^{62}Ni$ ratios due to $^{46}Ti^{16}O$ and $^{46}Ca^{16}O$ interferences on nickel-62. Regardless, as noted above, we measured the nickel-62 peak ~−1.2 mamu off center, and we avoided Ti- and/or Ca-rich areas within the measurement fields, to minimize the effect of the tails of the $^{46}Ti^{16}O$ and $^{46}Ca^{16}O$ peaks.

3.3. Transmission Electron Microscopy

Electron-transparent slices of a calcium-rich chondrule pyroxene from MET 00526 (chondrule b1), a cryptocrystalline chondrule from QUE 97008 (b9) and a granular olivine chondrule from DOM 08006 (b49) were prepared after NanoSIMS analysis with an FEI Nova 600 Nanolab dual-beam focused ion beam instrument (FIB-SEM) at the Max Planck Institute for Polymer Research (Mainz, Germany). The FIB slices were then investigated with the aberration-corrected (objective system) FEI/ThermoFisher Scientific "Themis" transmission electron microscope (TEM) at the UM. The acceleration voltage was 300 kV. This TEM is equipped with a high-brightness field emission gun (X-FEG), a Wien-filter type monochromator, a four-quadrant silicon-drift EDX detector (SuperX technology), a Fischione Model 6000 high-angle annular darkfield (HAADF) detector, and a fast CMOS camera (Ceta 4 k × 4 k). We performed conventional brightfield, high-resolution imaging, and selected area electron diffraction (SAED) to document the texture and crystallography of studied samples. Spectrum images were acquired in scanning TEM (STEM) mode (condensor aperture 50 μm) using beam currents of about 500–800 pA and analysis times of 100–200 μs px^{-1}, with several hundred frames summed to achieve sufficient counting statistics. We quantified TEM-EDX data using the Velox software (ThermoFisher).

4. Results

4.1. Petrography

4.1.1. General Observations

The analyzed objects are porphyritic olivine, porphyritic olivine-pyroxene, granular olivine, barred olivine, or cryptocrystalline chondrules (Table 1). The longest diameters of the analyzed objects in our CC chondrite samples are between 140 and 600 μm, which is shorter than the chondrules analyzed in our UOC samples (1000–2600 μm). Nevertheless, the sizes of the studied chondrules are not fundamentally different from those of other chondrules within their host samples.

Some of the studied chondrules exhibit zoning in mineralogy and/or mineral chemistry (Figure 2), which could influence the interpretation of isotope data. Zoning occurs either as diffuse chemical zoning in idiomorphic or hypidiomorphic phenocrysts (with the crystal cores being more magnesian than their rims; Figures 2(a) and (b)), or as mineral and chemical zoning whereby olivine is mantled by chemically zoned or unzoned enstatite (Figure 2(c), (d)), which in turn is surrounded by calcium-rich pyroxene (Figure 2(e)). Olivine crystals in assemblages with mineral zonation have irregular, curvilinear grain boundaries (Figure 2(b)), and can be skeletal crystals that represent the earliest member of a single crystallization sequence from olivine to calcium-rich pyroxene, or they can be a remnant, partially resorbed crystals from a previous chondrule generation. In both cases of mineralogical zonation (b1 and b20 from NWA 8276), we analyzed the iron-nickel isotope composition of enstatite, but not that of olivine or calcium-rich pyroxene because the origin of the former is uncertain, and because the thickness of the latter (usually <5 μm in thickness) is often insufficient for multiple isotope analyses.

Fissures and veins (i.e., filled fissures) are ubiquitous in the studied chondrules. Their thickness varies from a few tens of nanometers to several microns. Many of the veins contain iron-$\pm$ nickel-rich material, so choosing NanoSIMS analysis spots preferably away from veins, as done here, seems indeed very important (see also Telus et al. 2016). The distribution of iron and nickel in veins can be best illustrated by chondrule b1 from MET 00526 (Figure 3(a)). It is often only iron that can be seen in the veins on SEM-EDX element maps (Figures 3(b)–(d)), but in some places veins occur with both iron and nickel (Figures 3(e)–(j)). Furthermore, the composite TEM-EDX element map of a vein from the same chondrule (Figure 3(j)) suggests that not even in a single vein is the distribution of iron and nickel uniform. High-angle annular darkfield imaging and TEM-EDX mapping have also revealed the presence of tens of nanometer wide veinlets that may not be visible in ion images. These veinlets are, however, dominated by sodium- rather than iron- and/or nickel-rich material (Figure 3(j)).

4.1.2. TEM Observations on Two Chondrules with Extremely High Fe/Ni Ratios

We performed a detailed petrographic analysis of the two chondrules with the highest measured Fe/Ni ratios (b49 from DOM 08006 and b9 from QUE 97008; see also Section 4.2.), to evaluate potential iron-nickel redistribution. Chondrule b49 from DOM 08006 is the fragment of a granular olivine chondrule with 1–2 μm wide and 2–10 μm long, rounded olivine crystals and silicate-dominated mesostasis (Figures 4(a)–(e)). The silicate mesostasis is glass-like and lacks long-range order as can be seen from the diffuse diffraction pattern (Figure 4(e)). Compound iron-sulfide + iron-oxide grains (Figures 4(c)–(d) and (f)), up to $\sim$1.5 μm in diameter, occur throughout the mesostasis, and form the third most abundant "phase" within the chondrule (they are two phases but they almost always occur together; Figures 4(c) and (f)). Some of these grains are nickel-rich (Figure 1). Small (diameter: 100–300 nm) idiomorphic chromite crystals occur in the mesostasis (Figure 4(g)) as well as in olivine. Xenomorphic, curved, and elongated crystals of a calcium- and phosphorous-rich phase, presumably apatite, were observed in the mesostasis only (Figure 4(g)). Their size is highly variable: their longest dimension can reach a micron, whereas their smallest dimension is often only 100–200 nm. Olivine and sometimes chromite contain small (diameter: a few tens of nanometers) oval objects that are silicon-rich relative to the hosts (cyan arrows in Figures 4(g) and (h)). These inclusions are probably melt inclusions.

Chondrule b9 from QUE 97008 is a cryptocrystalline chondrule that was also studied by Telus et al. (2018). In the BSE images, the chondrule shows two markedly different textures. Along its rims and some of the numerous fissures that cut through it, the chondrule appears to consist of small (diameter 1–2 μm) grains that are surrounded by holes. We refer to this texture as porous (Figure 5(a), (b)). In the chondrule's core, there seem to be no holes between the small grains. We call the texture of these areas nonporous. All isotope measurement points were at areas that have nonporous texture (Figure 5(c)). According to the HAADF imaging and TEM-EDX data, the framework of both textures are slightly elongated or isometric, round olivine crystals of 1–2 μm size (longest diameter). The olivines have oval inclusions that are richer in silicon and aluminum than their host. These are probably melt inclusions. The olivine crystals are discontinuously mantled by calcium-rich pyroxene (Figures 5(d)–(f)). In chondrule material with nonporous texture, there is silicate glass, iron-nickel metal, and iron sulfide between the pyroxene-mantled olivines (Figure 5(e)). Nickel is concentrated in the 100–200 nm large metal grains (Figure 5(e)). In contrast, in chondrule material with porous texture, the calcium-rich pyroxene mantles are less pronounced, the silicate glass and metal are missing, and nickel is concentrated on the edges of the voids left after the removal of silicate glass and metal (Figure 5(f)). The voids are sometimes filled with fibrous material (one example is outlined by a white dotted curve in Figure 5(f)).

4.2. Mineral Chemistry

A representative set of major and minor element compositions of the minerals chosen for isotope analysis is provided in Table 3. Table 1 also contains information about the chemistry of the mafic phases (i.e., $\mathrm{Mg\#} = 100 \times \mathrm{Mg}/(\mathrm{Mg+Fe+Mn+Ni})_{\mathrm{atomic}}$).

The analyzed mafic silicates span a wide range of compositions. Generally, our UOCs contain more type II chondrules (i.e., chondrules with mafic phases having $<$90 mole% magnesian end member; Lauretta et al. 2006) than our CO3 and CR3 samples, yet the least magnesian mafic silicates were found in our carbonaceous chondrite samples. The most iron-rich silicate studied here was the olivine of chondrule b49 of DOM 08006, with an average Mg# of 42 (Table 1). The Fe/Ni ratios estimated from NanoSIMS data vary between 79 ± 1 and $62{,}355 \pm 3624$ with the median at 6469. We found no

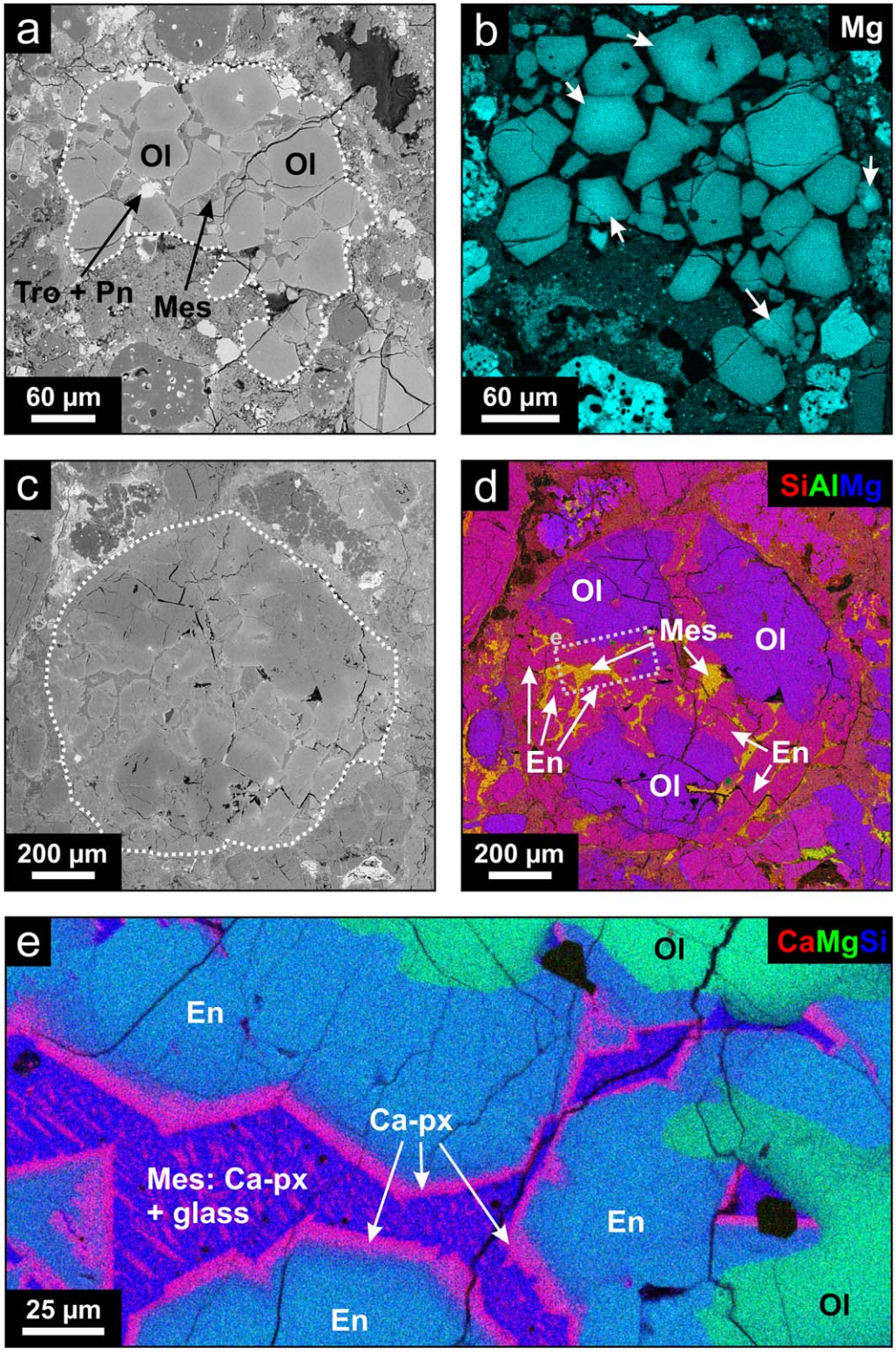

Figure 2. Chemical and mineral zoning in chondrules. Abbreviations are the same as in Figure 1, and as follows: Tro = troilite, Pn = pentlandite. (a) BSE image of chondrule b47 from DOM 08006. The chondrule outline is marked with a white stippled curve (b). Magnesium element map of the chondrule displayed in (a). Brightness scales with magnesium concentration. Diffuse magnesium zoning characterizes all olivine crystals, with crystal cores being richer in magnesium than rims, but due to differences in the position of the thin section's plane relative to the true cores of the crosscut olivine crystals, only a few show magnesium zoning strong enough to be clearly visible in the map (white arrows). (c) BSE image of chondrule b1 from NWA 8276. Chondrule outline is marked with a white stippled curve. (d) Composite aluminum–magnesium–silicon element map of the chondrule displayed in (c). Olivine forms large masses which are surrounded by enstatite. (e) Calcium-aluminum-silicon element map of a detail of the chondrule displayed in (c) and (d). Olivine is surrounded by enstatite. Calcium-rich pyroxene lines the boundary between enstatite and the mesostasis, and occurs in the mesostasis as well.

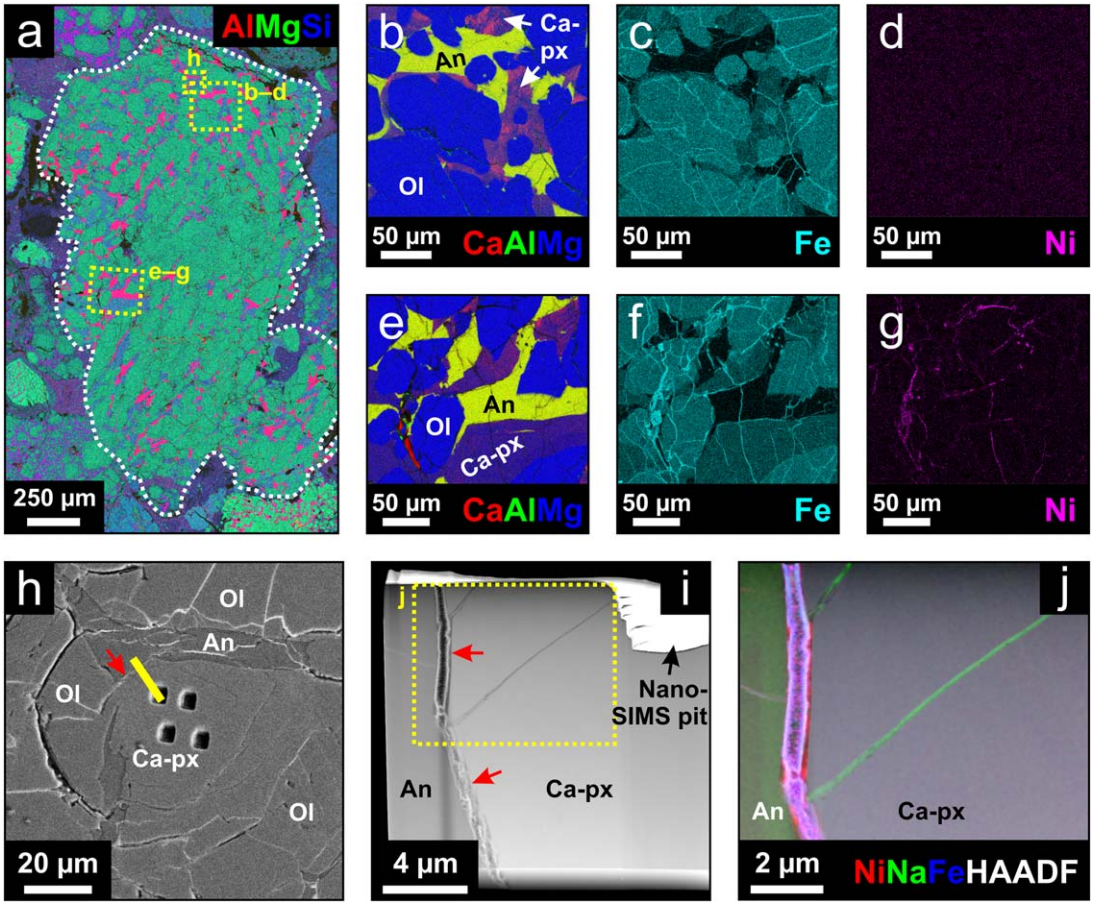

Figure 3. Veins in chondrule b1 of MET 00526. Abbreviations are the same as in Figure 1. (a) Aluminum–magnesium–silicon element map of the entire chondrule. (b)–(d) and (e)–(g) show element maps of two different areas within the chondrule displayed in (a). Both areas have a dense network of iron-rich veins, while their nickel distributions are markedly different. (h) BSE image of a third detail of the chondrule, with NanoSIMS analysis pits (see also Figure 1). Yellow line shows the trace of the FIB slice shown in (i) and (j). Red arrow points at the vein also highlighted by red arrows in (i). (i) HAADF image of the FIB slice cut along the yellow line in (h). The high-Z material filling the NanoSIMS pit is platinum from the FIB sample preparation. (j) Nickel–sodium–iron element map combined with the HAADF image of a detail of the FIB slice shown in (i). Notice the partial decoupling of nickel and iron in the major, thick vein on the left-hand side of the image, and the sodium-rich *satellite* veinlets.

correlation between the analyzed mafic phases' Mg# and Fe/Ni ratio (Table 1).

The anorthites selected for aluminum–magnesium isotope measurements are almost pure, with <3.6 mole% albite, and they have no detectable potassium (Table 3). The analyzed anorthites commonly have a silicon excess (0.05 excess silicon, on average, per 8 oxygens after accounting for the silicon in anorthite and albite components), and contain several tenths of weight percent (up to 0.93 wt.%) MgO and similarly high amounts of FeO.

4.3. Aluminum–magnesium Isotope Compositions

Inferred initial $^{26}Al/^{27}Al$ ratios of five UOC chondrules (Table 4) were calculated from the difference between the $^{26}Mg/^{24}Mg$ ratios of a high and a low Al/Mg phase (anorthite or silicate mesostasis and olivine or enstatite, respectively) in each. Thus, they are not derived from isochrons. In only three of the five analyzed chondrules could the former presence of aluminum-26 be verified with high certainty. In these chondrules (b1 of MET 00526, b16 of QUE 97008, and b20 of NWA 8276), inferred $^{26}Al/^{27}Al$ ratios are higher than four times the respective analytical uncertainty. Using the half-life determined by Norris et al. (1983), 705 (±24) kyr, these three chondrules formed 1.36+0.21/−0.18, 1.13+0.23/−0.19, and 1.52+0.25/−0.20 Myr after CCAIs ($^{26}Al/^{27}Al = 5.25 \times 10^{-5}$; Larsen et al. 2011).

4.4. Iron-nickel Isotope Compositions

Standardized $^{60}Ni/^{62}Ni$ and $^{56}Fe/^{62}Ni$ ratios together with raw $(^{46}Ca + {}^{46}Ti)/^{62}Ni$ ratios are listed in Table 5. Figures 6(a) and (b) show the $^{60}Ni/^{62}Ni$ and $^{56}Fe/^{62}Ni$ ratios. $^{60}Ni/^{62}Ni$ ratios vary between 6.68 ± 0.26 and 7.89 ± 0.38. Six of ninety-one $^{60}Ni/^{62}Ni$ data listed in Table 5 are anomalous at the 95% but none at the 99.7% or higher confidence level (six ratios deviate from the terrestrial $^{60}Ni/^{62}Ni$ ratio by $>2\sigma$ but none by 3σ or more; the terrestrial ratio is 7.215 ± 0.003; Gramlich et al. 1989). Interestingly, all of these anomalous ratios are subterrestrial, which is unexpected if the data reflected only stochastic variations around the terrestrial or a superterrestrial composition. In such a case there should be $>2\sigma$ superterrestrial $^{60}Ni/^{62}Ni$ ratios in our data set, too. The weighted average $^{60}Ni/^{62}Ni$ ratio of the entire data set is also subterrestrial: 7.183 ± 0.010 (MSWD = 1.01; MSWD: mean squared weighted deviation, also known as reduced χ^2).

The data points of individual chondrules in Figure 6 do not form isochrons. Instead, they tend to show scattered patterns, regardless of whether their $^{56}Fe/^{62}Ni$ ratios span a large or a

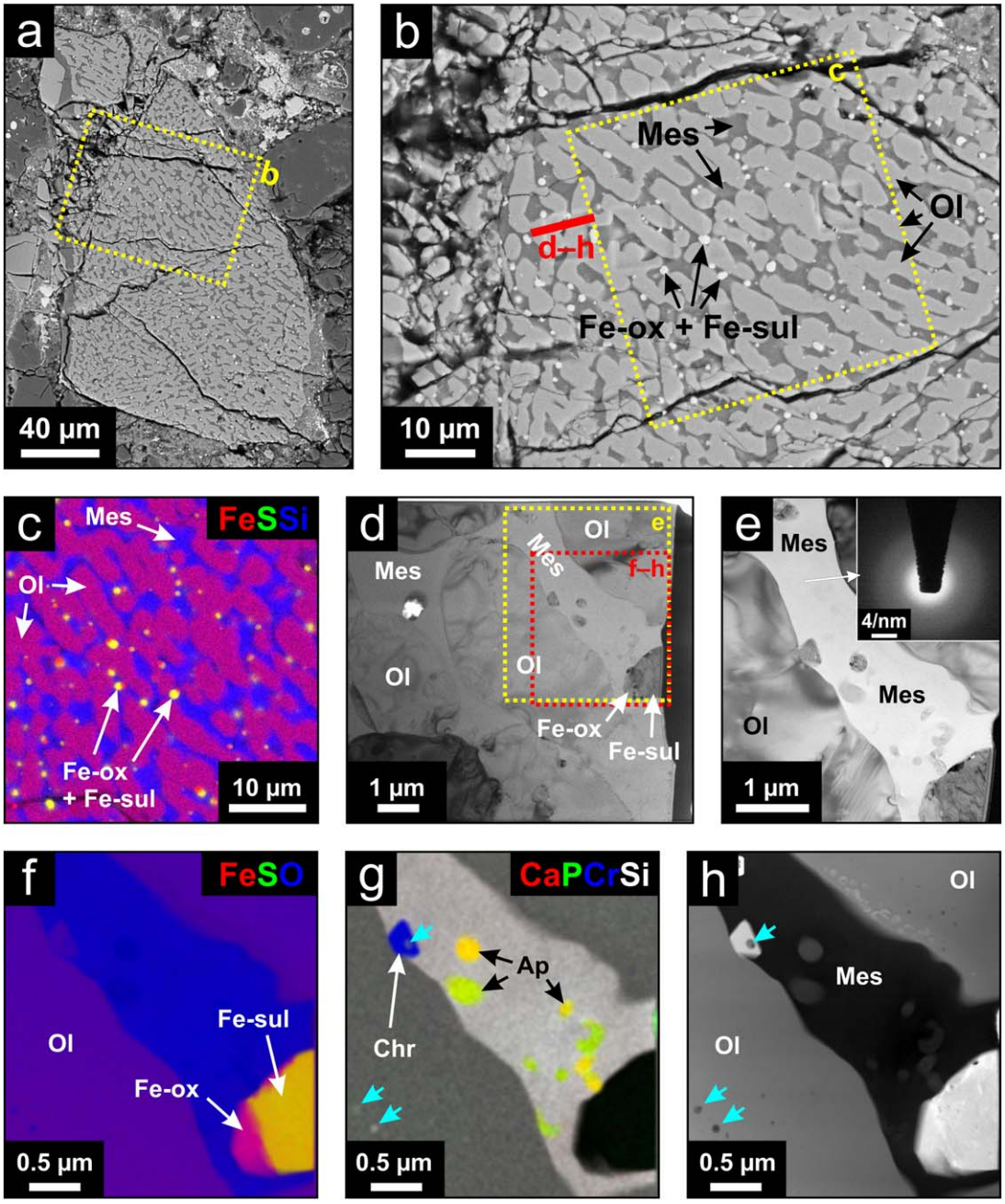

Figure 4. Texture and phase assemblage of chondrule b49 from DOM 08006. Abbreviations are the same as in Figure 1, with the following additions: Ap = apatite, Chr = chromite. (a) BSE image of the entire chondrule fragment with the area shown in (b) indicated by a yellow dotted rectangle. (b) BSE image of a chondrule detail. The location where the FIB slice shown in (d–h) was lifted out is indicated by a red line. Yellow dotted rectangle shows the area displayed in (c). (c) Composite iron-sulfur–silicon element map of the area indicated in (b). Notice the association of ~1 μm bright yellow iron-sulfide (Fe-sul) grains with red iron-oxide (Fe-ox) grains of about the same or smaller size. (d) Brightfield image of the FIB slice lifted out of the chondrule (see (b) for the exact location). Yellow and red dotted rectangles indicate the areas depicted in (e) and (f)–(h), respectively. (e) Brightfield image of a detail of the FIB slice, with the SAED pattern of the silicate mesostasis in the inset. (f) Composite iron-sulfur–oxygen element map of the area shown in (e). (g) Composite calcium–phosphorous–chromium–silicon element map of the area shown in (e). Cyan arrows indicate what are presumably melt inclusions. (h) HAADF image of the area shown in (e). Again, cyan arrows indicate what are presumably melt inclusions.

small range. The scatter reflects at least partially the low precision of many of our measurements. In Section 5.3, we will show that some of the scatter may result from mass-dependent isotope fractionation during parent body history or before. In addition, in some of the analyzed chondrules, only a few measurement points could be placed. Weighted linear regression of $^{60}Ni/^{62}Ni$ versus $^{56}Fe/^{62}Ni$ data from individual chondrules to determine initial $^{60}Fe/^{56}Fe$ ratios is therefore challenging, and in many cases does not promise a sensible outcome. Nevertheless, we performed weighted linear regression (Mahon 1996) in six chondrules with eight or more data each. In the case of chondrule b46 from DOM 08006, troilite data of Kodolányi et al. (2022) from the same chondrule were also included. All but one of these regressions yielded initial $^{60}Fe/^{56}Fe$ ratios that were distinguishable from 0 at the 95% confidence level. The only exception is chondrule b15 from NWA 8276, for which linear regression gave a negative slope in the $^{60}Ni/^{62}Ni$ versus $^{56}Fe/^{62}Ni$ space (-1.01 (± 0.43) $\times 10^{-6}$,

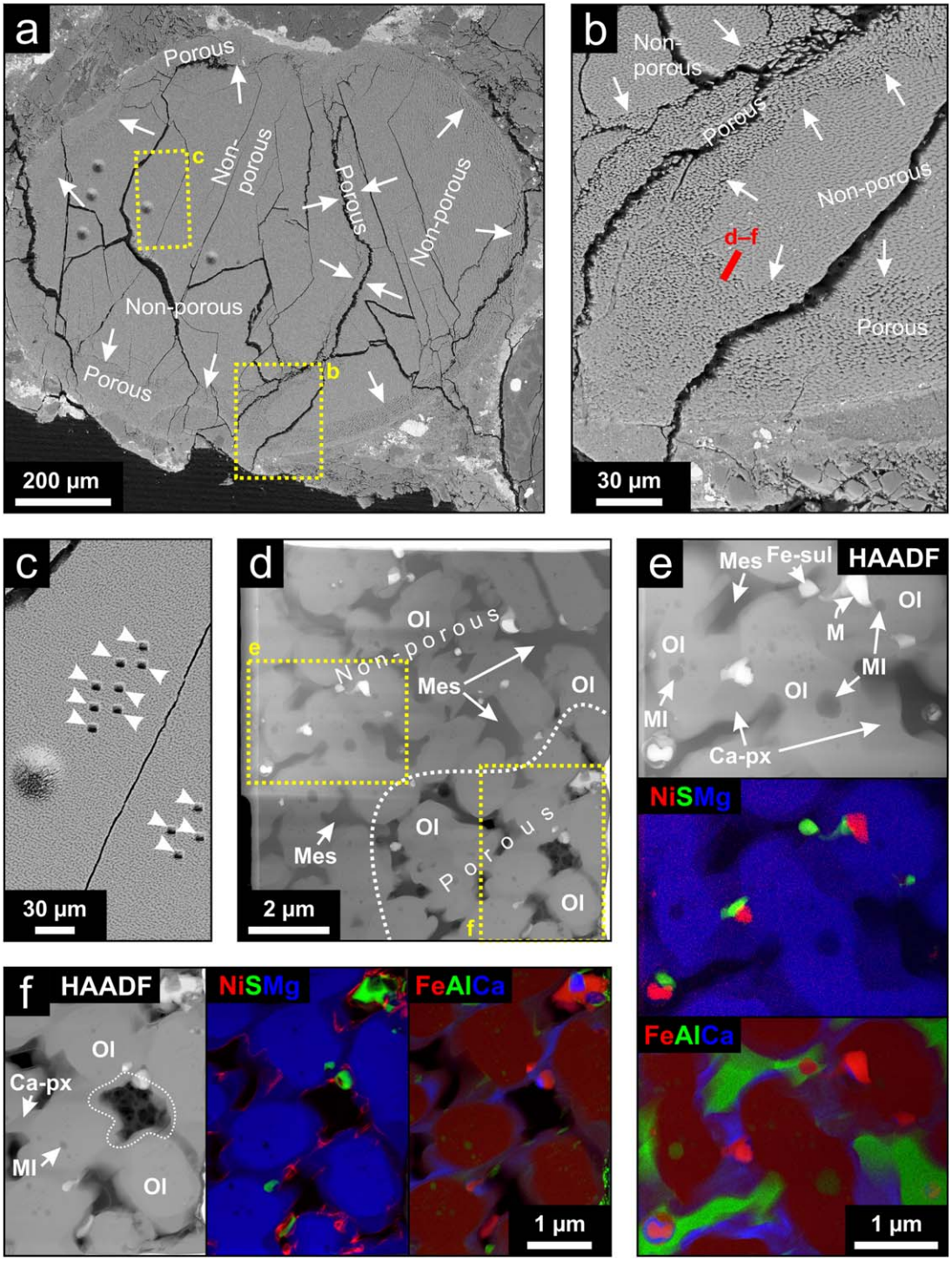

Figure 5. Texture and phase assemblage of chondrule b9 from QUE 97008. Abbreviations are the same as in Figure 1, with the following additions: M = iron-nickel metal, MI = melt inclusion. (a) BSE image of the entire chondrule with the areas shown in (b) and (c) indicated by yellow dotted rectangles. White arrows point at the boundary between areas with nonporous and porous textures (see also (b)). (b) BSE image of a detail of the chondrule, with the red line indicating the location of the FIB slice lifted out from the boundary between material with nonporous and porous textures (the boundary is again marked with white arrows). (c) BSE image of another detail of the chondrule, that shows the analysis points of the present study (10 sample and two dynamic background measurements, all marked with white arrowheads) and one from the study by Telus et al. (2018 large circular pit). All of the points are in the nonporous part of the chondrule. (d) HAADF image of the FIB slice from the boundary between nonporous and porous chondrule parts. White dotted curve is the approximate trace of the actual boundary. The thin section's surface was toward the right. (e) HAADF image and composite element maps of a detail of the FIB slice shown in (d). Nonporous texture. (f) HAADF image and composite element maps of a detail of the FIB slice shown in (d). Porous texture.

$n = 8$, MSWD = 1.68). This is inconsistent with in situ iron-60 decay.

Instead of using individual chondrules for linear regression, we can also use the $^{60}Ni/^{62}Ni$ and $^{56}Fe/^{62}Ni$ ratios of different chondrules from the same or many different meteorites to calculate the average initial $^{60}Fe/^{56}Fe$ ratios (Kodolányi et al. 2022). This approach is justified by the fact that the overwhelming majority (85%) of dated UOC, CO, and

Table 3
Representative Set of Olivine, Pyroxene, and Plagioclase Compositions

Sample	Chondrule	Mineral	Measurement	Technique	SiO2 (wt. %)	±	Al2O3 (wt.%)	±	Cr2O3 (wt.%)	±	TiO2 (wt. %)	±	MgO (wt. %)	±
DOM 08006	b47	Olivine	#8	EDX	35.51	0.15	b.d.l.		0.30	0.06	b.d.l.		28.19	0.12
	b49	Olivine	#453	EDX	33.39	0.14	0.09	0.05	0.25	0.05	b.d.l.		18.89	0.10
ALHA77307	b13	Olivine	#7	EPMA	37.710	0.275	0.009	0.017	0.166	0.032	0.049	0.058	34.410	0.203
MET 00426	b1	Olivine	#3	EPMA	36.960	0.274	0.018	0.017	0.389	0.039	b.d.l.		32.170	0.196
MET 00526	b1	Ca-rich pyroxene	#9	EDX	52.93	0.15	2.83	0.06	1.28	0.07	0.52	0.05	24.84	0.10
		Anorthite	#3	EDX	45.26	0.14	34.06	0.11	b.d.l.		b.d.l.		0.80	0.04
QUE 97008[a]	b9	Cryptocrystalline chondrule average ($n = 3$)	#33–#35	EDX	47.25	0.22	2.28	0.04	0.73	0.05	0.28	0.25	26.44	0.22
	b16	Enstatite	#11	EDX	55.19	0.16	1.09	0.05	1.03	0.06	0.14	0.05	29.92	0.10
	b16	Anorthite	#4	EDX	44.90	0.14	34.31	0.11	b.d.l.		b.d.l.		0.74	0.04
NWA 8276	b1	Enstatite	#10	EPMA	54.190	0.179	0.414	0.021	0.985	0.038	0.034	0.022	25.650	0.136
	b15	Olivine	#8	EPMA	39.540	0.158	0.003	0.013	0.500	0.029	0.005	0.022	43.580	0.174

Sample	Chondrule	Mineral	Measurement	Technique	CaO (wt.%)	±	P_2O_5 (wt.%)	±	MnO (wt.%)	±	FeO (wt.%)[b]	±	NiO (wt.%)	±
DOM 08006	b47	Olivine	#8	EDX	0.49	0.04	b.d.l.		0.26	0.07	35.25	0.18	b.d.l.	
	b49	Olivine	#453	EDX	0.67	0.04	0.30	0.05	0.69	0.07	45.71	0.17	b.d.l.	
ALHA77307	b13	Olivine	#7	EPMA	0.281	0.013	0.006	0.014	0.282	0.055	27.270	0.376	0.028	0.026
MET 00426	b1	Olivine	#3	EPMA	0.273	0.013	0.060	0.017	0.489	0.066	29.940	0.392	0.055	0.026
MET 00526	b1	Ca-rich pyroxene	#9	EDX	9.20	0.07	b.d.l.		0.30	0.06	8.09	0.11	b.d.l.	
		Anorthite	#3	EDX	18.92	0.09	b.d.l.		b.d.l.		0.79	0.07	b.d.l.	
QUE 97008[a]	b9	Cryptocrystalline chondrule average ($n = 3$)	#33–#35	EDX	1.44	0.18	0.15	0.13	0.59	0.06	19.05	0.13	b.d.l.	
	b16	Enstatite	#11	EDX	2.35	0.04	b.d.l.		0.18	0.06	10.10	0.12	b.d.l.	
	b16	Anorthite	#4	EDX	19.04	0.09	b.d.l.		b.d.l.		0.64	0.07	b.d.l.	
NWA 8276	b1	Enstatite	#10	EPMA	0.552	0.014	0.0002	0.012	0.495	0.027	17.620	0.171	0.001	0.014
	b15	Olivine	#8	EPMA	0.076	0.009	b.d.l.		0.574	0.028	16.250	0.166	0.006	0.014

Sample	Chondrule	Mineral	Measurement	Technique	CoO (wt.%)	±	Na_2O (wt.%)	±	K_2O (wt.%)	±	S (wt.%)	±
DOM 08006	b47	Olivine	#8	EDX	b.d.l.		b.d.l.		b.d.l.		b.d.l.	
	b49	Olivine	#453	EDX	b.d.l.		b.d.l.		b.d.l.		b.d.l.	
ALHA77307	b13	Olivine	#7	EPMA	0.047	0.024	b.d.l.		b.d.l.		n.a.	
MET 00426	b1	Olivine	#3	EPMA	0.055	0.024	0.025	0.041	n.a.		n.a.	
MET 00526	b1	Ca-rich pyroxene	#9	EDX	b.d.l.		b.d.l.		b.d.l.		b.d.l.	
		Anorthite	#3	EDX	b.d.l.		0.17	0.03	b.d.l.		b.d.l.	
QUE 97008[a]	b9	Cryptocrystalline chondrule average ($n = 3$)	#33–#35	EDX	b.d.l.		1.45	0.02	0.21	0.01	0.12	0.02
	b16	Enstatite	#11	EDX	b.d.l.		b.d.l.		b.d.l.		b.d.l.	
	b16	Anorthite	#4	EDX	b.d.l.		0.39	0.03	b.d.l.		b.d.l.	
NWA 8276	b1	Enstatite	#10	EPMA	b.d.l.		b.d.l.		0.002	0.003	n.a.	
	b15	Olivine	#8	EPMA	0.005	0.014	b.d.l.		0.001	0.003	n.a.	

Notes. b.d.l. = below detection limit; n.a. = not analyzed.
[a] Uncertainties for QUE 97008 b9 data are standard deviations of three measurements, each covering a 30 μm diameter circular area.
[b] All iron is reported as FeO.

Table 4
Inferred Initial $^{26}Al/^{27}Al$ Ratios and Crystallization Ages of Selected Chondrules

Meteorite	Chondrule	Analyzed Phase	$^{27}Al/^{24}Mg$	±	$^{26}Al/^{27}Al \times 10^5$	±	Age After CCAIs (million yr)[a]	$+/-$[b]
MET 00526	b1	Anorthite	56.9	0.1	1.38	0.26	1.36	0.21/0.18
QUE 97008	b15	Anorthite	63.7	1.5	0.67	0.53	2.09	1.54/0.59
QUE 97008	b16	Anorthite	57.4	1.8	1.73	0.35	1.13	0.23/0.19
NWA 8276	b1	Mesostasis	151.3	0.6	0.12	0.21	3.88	−/1.04
NWA 8276	b20	Mesostasis	149.0	0.8	1.18	0.25	1.52	0.25/0.20

Notes. NanoSIMS data. All quoted uncertainties represent a 68% confidence level.
[a] Calculated using a ^{26}Al half-life of 0.705 million yr and an initial $^{26}Al/^{27}Al$ ratio of 5.25×10^{-5} in the CCAI reservoir.
[b] Uncertainties do not include the uncertainty of the half-life.

CM chondrules formed within an about 1 Myr time window between 1.81 and 2.70 (CC chondrules), and between 1.68 and 2.75 Myr (NC chondrules) after the formation of CCAIs (based on data from Rudraswami & Goswami 2007; Kurahashi et al. 2008; Villeneuve et al. 2009; Ushikubo et al. 2013; Hertwig et al. 2019; Pape et al. 2019; Siron et al. 2021, and Fukuda et al. 2022 see also Section 5.6), and this is much shorter than the half-life of iron-60 (2.62 Myr, see Section 1), so the two chondrule forming regions should have lost only 20%–25% of their iron-60 to decay during this time interval. For our entire data set, the calculated average initial $^{60}Fe/^{56}Fe$ ratio is 12.4 ($\pm$6.7) $\times 10^{-8}$, $n = 91$, MSWD = 0.98 (regression [1] in the right panel of Figure 7(a)). Linear regression of our data from CC and NC meteorites separately gives average initial $^{60}Fe/^{56}Fe$ ratios of 2.8 ($\pm$1.3) $\times 10^{-7}$ ($n = 33$, MSWD = 1.04), and 4.8 ($\pm$9.8) $\times 10^{-8}$ ($n = 58$, MSWD = 0.94), respectively (yellow and blue symbols above regressions with number [1] in the left and center panels of Figure 7(a), respectively).

5. Discussion

5.1. Pristine Chondrules

The presence of different kinds of zoning (Figure 2) in some but not all chondrules within the same meteorite, and the preservation of glassy mesostasis and melt inclusions (Figures 4 and 5), suggest that the analyzed chondrules have escaped thermal metamorphism, consistent with the host meteorites' petrologic types (~3; Table 1). Chondrule minerals and glassy mesostasis were not replaced pseudomorphically by new phases upon interaction with aqueous fluids, even though abundant veins attest to the presence of fluids during the history of the meteorites. Veins with a few hundred nanometer diameter were found to contain iron- and/or nickel-rich material (Figure 3) with likely variable Fe/Ni ratios. Such veins are easily recognizable in ion images and avoided during data reduction. Veins with smaller diameter (i.e., $d < 100$ nm), which could not be resolved by our measurements (unless the veins in question run ~parallel to the thin section's surface), may or may not contain iron and/or nickel in sufficient quantities to influence isotope measurements. Our limited observations suggest that such veins are not iron- or nickel-rich (Figure 3(j)).

Based on our micro and nanoscale observations, the studied chondrules represent pristine material that did not undergo thermal metamorphism or aqueous alteration. This and the fact that analysis in the imaging mode of NanoSIMS with 200–300 nm spatial resolution is sufficient to avoid most veins that contain abundant iron or nickel give us confidence that measured isotope compositions are the result of radioactive decay and processes that took place before the chondrules' incorporation in their parent bodies.

5.2. Inferred Chondrule Ages

All five chondrules we dated using the aluminum–magnesium isotope chronometer are from UOC chondrites (Tables 1 and 4). The weighted average initial $^{26}Al/^{27}Al$ ratio of the five chondrules is 8.87 ($\pm$1.23) $\times 10^{-6}$, which corresponds to an average formation age of 1.81+0.15/−0.13 Myr after the formation of CCAIs (using 5.25×10^{-5} as the canonical $^{26}Al/^{27}Al$ ratio, and 705,000 yr as the half-life of ^{26}Al; Norris et al. 1983; Larsen et al. 2011). This average age is consistent with the frequency peaks of anorthite-bearing and anorthite-free UOC chondrule ages at ~1.9 and ~2 Myr after CCAIs, respectively (Pape et al. 2019; Siron et al. 2021). However, two of the five chondrules dated here have inferred initial $^{26}Al/^{27}Al$ ratios exceeding 10^{-5} by more than 1σ, whereas UOC chondrules with similarly high initial $^{26}Al/^{27}Al$ ratios are rare in the available record (three out of 76 based on the data of Rudraswami & Goswami 2007; Villeneuve et al. 2009; Pape et al. 2019, and Siron et al. 2021). Finding two such chondrules in a "random" set of five is unlikely ($p \approx 0.014$, using the above statistics and assuming binomial distribution).

The apparent overabundance of chondrules with high inferred initial $^{26}Al/^{27}Al$ ratios in our data set could be the result of aluminum loss from the anorthite and mesostasis, or of the underestimation of the a factor of QSA correction (see Section 3). However, the chemistry of the anorthites analyzed here is typical of pristine, unmetamorphosed chondrule anorthite: it has several tenths of wt.% MgO and FeO, as well as silicon excess (Table 3; Kurahashi et al. 2008). We also could not find traces of aluminum loss in the two mesostases analyzed for their aluminum–magnesium isotope composition. Thus, the most likely explanation for the overestimation of $^{26}Al/^{27}Al$ ratios of our chondrules is the underestimation of the a factor used in the QSA correction. For instance, using the 1σ upper limit of the a factor to correct the $^{25}Mg/^{24}Mg$ ratios of the oldest chondrule dated here, b16 from QUE 97008, results in a calculated initial $^{26}Al/^{27}Al$ ratio of 1.34 ($\pm$0.34) $\times 10^{-5}$, instead of the 1.73 ($\pm$0.35) $\times 10^{-5}$ listed in Table 4. If we adopt the increased a factor for all chondrules from Table 4, there would be no $^{26}Al/^{27}Al$ ratios exceeding 10^{-5} by more than 1σ. Nevertheless, as shown by the above example, an increased a factor would still not push calculated $^{26}Al/^{27}Al$ ratios to a level that would suggest the analyzed chondrules were significantly *younger* than UOC chondrules in general.

Table 5
Isotope Ratios of Chondrule Silicate Phases

Sample	Chondrule	Mineral	Measurement	$^{56}Fe/^{62}Ni$[a]	±	$^{60}Ni/^{62}Ni$	±	$(^{46}Ti + {}^{46}Ca)/^{62}Ni$[b]	±
DOM 08006	b46	Olivine	1_olx4	155,901	4687	7.2560	0.2065	7.6	0.2
		Olivine	1_olx5	145,188	4851	6.9715	0.2265	6.8	0.2
		Olivine	2_olx1	230,796	6693	7.2171	0.1769	11.3	0.3
		Olivine	2_olx2	279,957	14,548	7.1009	0.3711	10.1	0.5
	b47	Olivine	olx1	15,169	327	7.2437	0.0572	0.49	0.01
		Olivine	olx3	21,939	167	7.2330	0.0590	0.52	0.01
		Olivine	olx4	20,526	161	7.1007	0.0568	0.47	0.01
	b49	Olivine	ol1	314,945	10,919	7.2271	0.2154	13.9	0.4
		Olivine	ol2	1,574,159	92,157	7.3696	0.4568	87	5
		Olivine	ol3	1,518,261	91,947	7.4020	0.4745	97	6
		Olivine	ol4	809,365	48,688	6.9021	0.4431	47	3
		Olivine	ol5	518,786	18,087	7.1304	0.2644	23	1
		Olivine	ol6	956,820	40,427	7.5965	0.3402	44	2
		Olivine	ol7	1,143,315	48,952	7.7964	0.3480	42	2
		Olivine	ol8	835,840	38,577	7.8896	0.3804	39	2
ALHA77307	b13	Olivine	olx1b	28,442	337	7.1097	0.0808	1.02	0.02
		Olivine	olx2	24,926	388	7.0513	0.1105	1.54	0.03
		Olivine	olx3	33,909	681	7.3527	0.1517	1.23	0.03
	b16	Olivine	ol1	53,808	1240	7.2736	0.1784	0.89	0.03
		Olivine	ol2	37,457	1751	7.3075	0.3641	0.50	0.04
		Olivine	ol2b	84,026	2883	7.2782	0.2678	0.89	0.04
		Olivine	ol3	66,088	2292	7.4710	0.2386	0.65	0.03
		Olivine	ol12	99,074	4092	7.5612	0.3013	1.6	0.1
MET 00426	b1	Olivine	ol3	20,195	282	7.1802	0.0764	0.49	0.01
		Olivine	ol4	18,058	255	7.1319	0.0775	0.39	0.01
		Olivine	ol9	19,627	275	7.1065	0.0763	0.44	0.01
		Olivine	ol9b	13,075	155	7.2460	0.0620	0.175	0.004
		Olivine	ol10	13,438	160	7.2642	0.0637	0.213	0.004
	b4	Olivine	ol1	2156	17	7.1359	0.0308	0.0158	0.0005
		Olivine	ol4	2003	15	7.1199	0.0297	0.0146	0.0004
		Olivine	ol5	2032	15	7.1463	0.0295	0.0170	0.0005
		Olivine	ol5b	2374	27	7.2319	0.0273	0.0148	0.0004
		Olivine	ol6	18,010	216	7.2246	0.0725	0.213	0.005
MET 00526	b1	Olivine	5_8-Fe	74,715	1086	7.0851	0.1130	18.3	0.3
		Ca-rich pyroxene	5_pxx1	94,747	1507	7.0669	0.1242	275	4
		Ca-rich pyroxene	5_pxx2	246,574	5324	7.2981	0.1688	608	13
		Ca-rich pyroxene	5_pxx3	255,634	5513	7.3614	0.1700	742	16
		Ca-rich pyroxene	5_pxx4	235,908	12,087	7.0257	0.3839	1106	56
		Ca-rich pyroxene	5_pxx4b	253,692	6628	7.1887	0.2009	1136	27
		Olivine	6_ol07	55,614	530	7.2296	0.0690	9.4	0.1
		Olivine	6_ol08	60,593	593	7.2279	0.0711	20.7	0.2
		Olivine	6_ol08b	45,856	415	7.1769	0.0646	11.0	0.1
		Olivine	6_olx1	47,294	420	7.1649	0.0632	20.6	0.2
		Ca-rich pyroxene	6_pxx1	29,522	594	7.0825	0.1530	249	4
		Ca-rich pyroxene	6_pxx2	311,975	7221	7.3928	0.1813	2487	57
		Ca-rich pyroxene	6_pxx3	291,533	6504	6.9321	0.1645	1900	42
		Ca-rich pyroxene	6_pxx4	293,709	6523	7.3475	0.1718	1651	36
		Ca-rich pyroxene	6_pxx5	68,496	1545	7.3249	0.1740	476	11
QUE 97008	b9	Crypt. phase mix.[c]	x1	472,534	10,025	7.0759	0.1597	315	7
		Crypt. phase mix.	x2	559,938	12,292	6.9934	0.1634	414	9
		Crypt. phase mix.	x3	807,627	21,442	6.9513	0.1968	584	15
		Crypt. phase mix.	x4	547,025	12,049	7.2153	0.1689	313	7
		Crypt. phase mix.	x5	1,117,282	37,624	7.3789	0.2476	736	23
		Crypt. phase mix.	x6	595,982	15,278	7.4244	0.1795	386	9
		Crypt. phase mix.	x7	1,335,792	47,489	7.6752	0.2870	1038	37
		Crypt. phase mix.	x8	532,586	10,765	7.2578	0.1517	309	6
		Crypt. phase mix.	x9	602,674	13,042	7.2884	0.1637	417	9
		Crypt. phase mix.	x10	502,202	9965	7.1305	0.1463	345	7
	b15	Enstatite	7_Enx1	162,114	3200	7.2646	0.1486	255	5
		Enstatite	7_Enx2	316,796	7163	7.2612	0.1713	554	12
		Enstatite	7_Enx4	130,141	2282	7.1357	0.1290	206	3
		Enstatite	7_Enx5	230,458	5562	7.5380	0.1854	353	8
		Enstatite	7_Enx6	219,391	5162	7.4173	0.1776	366	8
	b16	Enstatite	13_pxx1	163,299	2759	7.0715	0.1257	204	3

Table 5
(Continued)

Sample	Chondrule	Mineral	Measurement	$^{56}Fe/^{62}Ni$[a]	±	$^{60}Ni/^{62}Ni$	±	$(^{46}Ti + {}^{46}Ca)/^{62}Ni$[b]	±
		Enstatite	13_pxx2	168,912	3658	7.1572	0.1367	215	4
		Enstatite	13_pxx3	158,946	3354	7.0426	0.1296	197	3
		Enstatite	13_pxx4	181,984	3940	7.0927	0.1354	261	4
		Enstatite	14_Enx1	176,927	3866	7.0354	0.1712	179	4
		Enstatite	14_Enx2	182,392	3981	7.3582	0.1718	187	4
		Enstatite	15_pxx1	139,876	2659	7.1642	0.1223	158	2
		Enstatite	15_pxx2	143,119	2710	7.2036	0.1223	163	2
		Enstatite	15_pxx3	145,801	4150	7.3440	0.1675	154	2
		Enstatite	15_pxx4	217,234	4863	7.1057	0.1439	190	4
NWA 8276	b1	Enstatite	Enx1	151,245	2624	7.1900	0.1227	22.1	0.3
		Enstatite	Enx2	168,320	2676	7.2591	0.1251	35	1
		Enstatite	Enx3	127,720	2115	7.3117	0.1088	24.1	0.3
		Enstatite	En8	163,474	2838	7.3447	0.1166	33.8	0.5
		Enstatite	En10	148,649	2125	7.2979	0.1135	32.5	0.5
	b15	Olivine	olx1	323,631	10,458	7.2027	0.1910	11.6	0.3
		Olivine	olx2	633,155	24,838	6.6828	0.2612	28	1
		Olivine	olx3	348,511	12,166	6.7394	0.2294	10.3	0.3
		Olivine	olx4	98,291	2426	7.0648	0.1157	2.73	0.05
		Olivine	olx4b	153,099	2836	7.0083	0.1357	8.00	0.15
		Olivine	olx4c	100,003	2760	7.4887	0.2173	1.60	0.06
		Olivine	olx5	124,086	1887	7.3998	0.1149	4.07	0.07
		Olivine	olx6	110,485	1338	7.2053	0.0870	3.72	0.05
	b20	Enstatite	Enx1	387,685	20,308	7.7577	0.4069	74	4
		Enstatite	Enx2	321,425	10,076	7.2920	0.2026	78	2
		Enstatite	Enx3	570,073	29,251	7.2807	0.3773	140	7
		Enstatite	Enx4	170,670	9097	7.3371	0.3221	45	2
		Enstatite	Enx5	164,034	8798	7.1470	0.3175	46	2

Notes. NanoSIMS data.
[a] Calculated from measured $^{54}Fe/^{62}Ni$ ratios, assuming terrestrial iron isotope compositions.
[b] Raw intensity ratios.
[c] Cryptocrystalline phase mixture (olivine, silicate glass, Fe-rich sulfide, apatite).

5.3. Mass-dependent Isotope Fractionation

There are three "surprising" features of our iron-nickel data that deserve scrutiny. First, all $^{60}Ni/^{62}Ni$ ratios in our data set that are anomalous relative to the terrestrial ratio at the 95% confidence level are subterrestrial. Second, there is a chondrule with a significantly negative inferred initial $^{60}Fe/^{56}Fe$ ratio (b15 of NWA 8276; see Section 4.4). Third, the average inferred initial $^{60}Fe/^{56}Fe$ ratio of our chondrules as a single set is $\sim 1.7\sigma$ higher than the ratio suggested by bulk analytical data in the literature or by our own in situ troilite measurements (Kodolányi et al. 2022). In the next sections, we show how the three "peculiarities" might be related, and explore the possibilities to improve the quality of our estimates of initial $^{60}Fe/^{56}Fe$ ratios.

Although some of the six $^{60}Ni/^{62}Ni$ ratios whose 2σ upper limits are below the terrestrial value (hereafter: anomalous $^{60}Ni/^{62}Ni$ ratios) may result from the stochastic variations of our measurement results around a value close to the terrestrial, some may in fact reflect mass-dependent isotope fractionation or indicate that the precision of our measurements was not correctly estimated. In particular, the three anomalous $^{60}Ni/^{62}Ni$ ratios from chondrule b4 of MET 00426 and the two anomalous $^{60}Ni/^{62}Ni$ ratios from chondrule b15 of NWA 8276 (Table 5, and points highlighted by green arrows in Figure 6) are probably outliers that are unrelated to iron-60 decay or stochastic variations, yet have large effects on calculated average $^{60}Ni/^{62}Ni$ and initial $^{60}Fe/^{56}Fe$ ratios. Trappitsch et al. (2018) reported mass-dependent nickel isotope anomalies in a Semarkona chondrule of up to $\sim 8\%$/amu (amu = atomic mass unit), with $^{60}Ni/^{62}Ni$ ratios below and above the terrestrial value all measured in the same chondrule. Although their data set does not reveal a significant correlation between Fe/Ni ratios and the sense or magnitude of isotope anomalies, three out of the four analyses in their data set with $^{60}Ni/^{62}Ni$ ratios $>2\sigma$ below the terrestrial ratio had $^{56}Fe/^{62}Ni$ ratios below 140,000, when in total only six out of their 16-member data set had similarly *low* $^{56}Fe/^{62}Ni$ ratios. Thus, material with lower Fe/Ni ratios seems more likely to have negative mass-dependent isotope anomalies than material with higher Fe/Ni ratios. The anomalous $^{60}Ni/^{62}Ni$ ratios from MET 00426 from our study are identical within analytical uncertainty and lie $\sim 10\%$ below the terrestrial ratio (Table 5; Figure 6(b)). Their associated $^{56}Fe/^{62}Ni$ ratios are uniformly low (~ 2000). Thus, their composition is consistent with mass-dependent isotope fractionation similar to that observed by Trappitsch et al. (2018), and should be removed from our data set before weighted linear regression. Removing the three anomalous data from our CC set results in an average calculated initial $^{60}Fe/^{56}Fe$ ratio of $2.1\ (\pm 1.3) \times 10^{-7}$ (MSWD = 0.83) for our CC chondrules and by extension to the CC isotope reservoir. This value is smaller than the $2.8\ (\pm 1.3) \times 10^{-7}$ estimated with the three anomalous isotope ratios included, and 0 within 2σ (regressions [2] and [1], respectively, in the left panel of Figure 7(a)). An alternative explanation for the occurrence of the three anomalous MET 00426 data may be the underestimation of the precision of our measurements. To mitigate this problem (which probably does

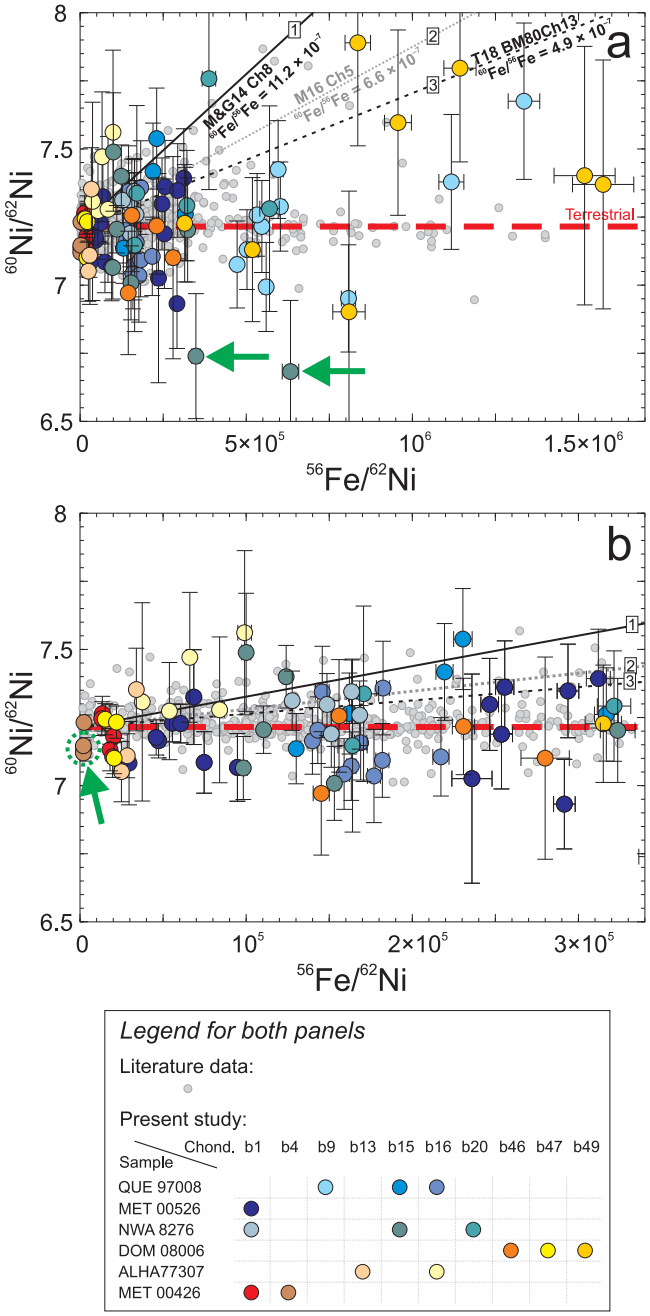

Figure 6. ^{56}Fe/^{62}Ni and ^{60}Ni/^{62}Ni ratios of chondrule silicates from the present study and the literature (Mishra & Goswami 2014 Mishra & Chaussidon 2014; Mishra et al. 2016; Telus et al. 2018). (a) The entire compositional range. (b) Data with ^{56}Fe/^{62}Ni ⩽ 340,000. Green arrows point at data points that are discussed in detail in Section 5.3 For data from the present study, ^{56}Fe/^{62}Ni ratios were calculated from ^{54}Fe/^{62}Ni ratios, assuming terrestrial iron isotope ratios, and error bars represent $\pm 1\sigma$. ^{56}Fe/^{62}Ni ratios from the literature were either reported as such in the original publications, or were recalculated from reported ^{56}Fe/^{61}Ni ratios (again under the assumption that iron isotope ratios were terrestrial), and error bars were omitted for legibility. Solid black lines (labeled "M&G14 Ch8" and/or "1") show the relationship between the ^{56}Fe/^{62}Ni and ^{60}Ni/^{62}Ni ratios expected for objects having the same initial ^{60}Fe/^{56}Fe ratios as that inferred for chondrule "8" from Semarkona by Mishra & Goswami (2014), 11.2×10^{-7}. Gray dotted lines (labeled "M16 Ch 5" and/or "2") show the same when calculated from the initial ^{60}Fe/^{56}Fe ratio of chondrule "Ch 5" from QUE 97008 (6.6×10^{-7}) inferred by Mishra et al. (2016). Finally, black short-dashed lines (labeled "T18 BM80 Ch13" and/or "3") correspond to ^{60}Ni/^{62}Ni versus ^{56}Fe/^{62}Ni ratios expected for objects having an initial ^{60}Fe/^{56}Fe ratio of 4.9×10^{-7}, inferred by Telus et al. (2018) for Bishunpur chondrule "BM80 Ch13". "Chond". in the legend stands for chondrule.

not exist, as we show below), one can normalize the entire nickel isotope data set to the average ^{60}Ni/^{62}Ni ratio of nickel-rich measurements, and increase the uncertainty of each datum accordingly. This normalization is justified because even if the studied chondrules had had high ^{60}Fe/^{56}Fe ratios at formation, e.g., an extreme value of 10^{-6}, those with the lowest ^{56}Fe/^{62}Ni ratios (i.e., <20,000) could not have developed ^{60}Ni/^{62}Ni ratios distinguishable from terrestrial by our analysis, even if we used several such measurements to calculate an average with reduced uncertainty. Thus, these measurements should scatter around the terrestrial isotope composition, and their scatter should reflect the true reproducibility of our measurements, provided the isotope fractionation discussed above did not affect our samples. Although the uncertainties do indeed increase after normalizing our nickel isotope data as described above, i.e., to the average ^{60}Ni/^{62}Ni ratio of those measurements that were paired with ^{56}Fe/^{62}Ni ratios <20,000 (7.174 ± 0.013; $n = 10$, MSWD = 1.85), they do not increase enough to render the high calculated average initial ^{60}Fe/^{56}Fe ratio of our CC silicates insignificant. The calculated ^{60}Fe/^{56}Fe ratio hardly changes because the slope of the regression line is still determined by the three anomalous data from MET 00426: $2.8\ (\pm 1.3) \times 10^{-7}$ (MSWD = 0.97; regression [3] in the left panel of Figure 7(a)). The only significant change after this exercise is, of course, that the intercept of the regression line at the y-axis shifts higher, from 7.170 ± 0.012 (subterrestrial) before renormalization to 7.212 ± 0.013 (terrestrial) after renormalization. We would like to point out that the weighted average used for the normalization above is strongly influenced by the three anomalous ^{60}Ni/^{62}Ni ratios from MET 00426. Without these ratios, the weighted average is terrestrial within uncertainty (7.223 ± 0.019; $n = 7$). Furthermore, the MSWD value of the weighted average without the anomalous ^{60}Ni/^{62}Ni ratios is well below one, at 0.75, whereas the weighted average that includes the anomalous data has an MSWD value of 1.85. This suggests that it is only the three anomalous data that increase the scatter of ^{60}Ni/^{62}Ni ratios in our most nickel-rich silicates. If we expand the group of data used to calculate the weighted average, and now use all ^{60}Ni/^{62}Ni ratios that are paired with ^{56}Fe/^{62}Ni ratios <50,000 (radiogenic ingrowth of nickel-60 still negligible), the weighted average is still dominated by those three anomalous data from chondrule b4 of MET 00426. The average, 7.171 ± 0.011 ($n = 20$), is identical to the weighted average calculated for data with ^{56}Fe/^{62}Ni ratios <20,000, and the MSWD value is again above one (1.21). Leaving out the three anomalous data lets again the average shift back to terrestrial within uncertainties (7.200 ± 0.015), and the MSWD value decreases again below one (0.91). Taken together, the three anomalous ^{60}Ni/^{62}Ni ratios measured in MET 00426 seem not to reflect stochastic variations but to be true outliers that most likely attest to mass-dependent isotope fractionation. Furthermore, the fact that removing the three anomalous isotope ratios results in terrestrial average ^{60}Ni/^{62}Ni ratios in minerals with the lowest ^{56}Fe/^{62}Ni ratios gives us confidence that the magnitude of instrumental mass fractionation uncorrected for by our matrix-matched standardization is insignificant.

Mass-dependent isotope fractionation may explain the anomalous ^{60}Ni/^{62}Ni ratios found in chondrule b15 from NWA 8276 as well. The ^{60}Ni/^{62}Ni ratios from these measurements ("olx2" and "olx3" in Table 5, points highlighted by green arrows in Figure 6(a)) are nominally more anomalous, and the

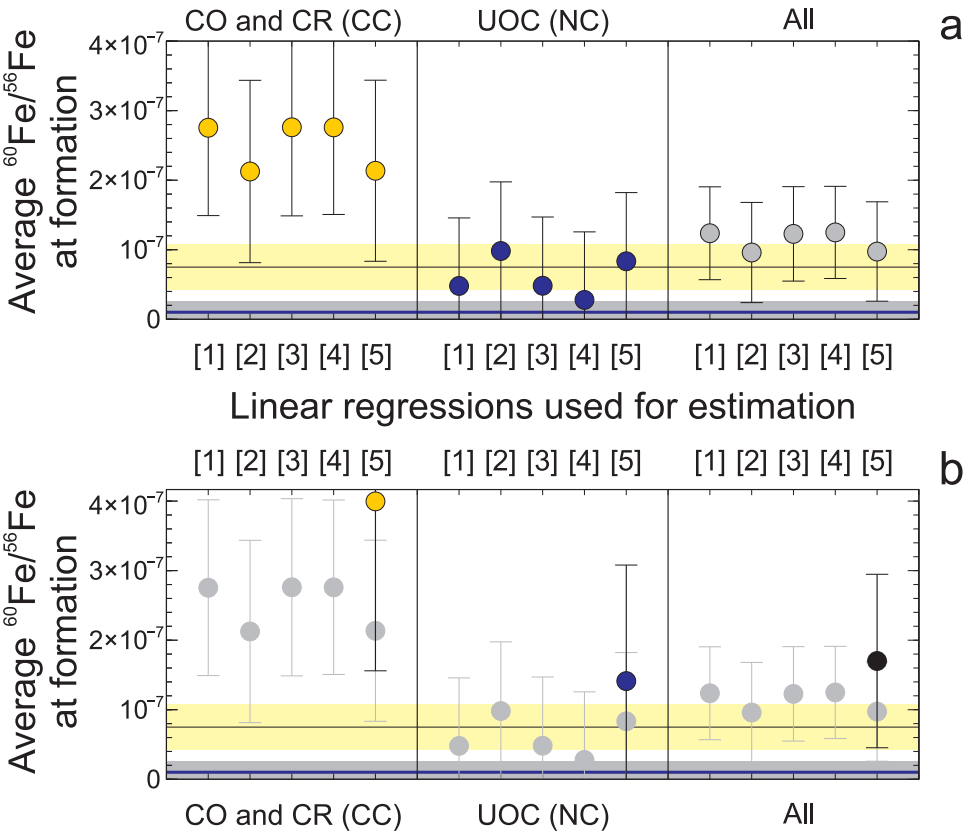

Figure 7. (a) Comparison of average initial ^{60}Fe/^{56}Fe ratios calculated from our CC (left panel), and NC (center panel) data, as well as the entire data set (right panel). Weighted linear regressions [1]–[5] were performed for each data set (indicated above or below each panel) similarly. [1] Regression based on all data of the given data set (Table 5), without consideration of correlations between uncertainties. [2] Regression based on data of the given data set minus the anomalous outliers discussed in Section 5.3, without considering correlations between uncertainties. [3] Regression of all data of the given data set after normalization of ^{60}Ni/^{62}Ni ratios to the average ^{60}Ni/^{62}Ni ratios of nickel-rich targets (^{56}Fe/^{62}Ni ratios <20,000) from the entire data set (i.e., not only from the data set for which the linear regression result is displayed). Correlations of uncertainties are again disregarded. [4] Regression based on all data of the given data set, with the effect of correlated uncertainties removed. [5] Regression based on data of the given data set minus the anomalous outliers discussed in Section 5.3, with the effect of correlated uncertainties removed. Thin black line with a light yellow band: initial ^{60}Fe/^{56}Fe of IVB iron meteorite precursors (CC isotope reservoir) according to Steele et al. (2012), with 1σ uncertainty. Thick blue line: ^{60}Fe/^{56}Fe$_{CCAI}$ ratio estimated by Tang & Dauphas (2015) (mostly) from quenched angrites, eucrites, and UOC chondrules (NC isotope reservoir). Line thickness was adjusted to cover ±1σ uncertainty. Gray band: uncertainty of the initial ^{60}Fe/^{56}Fe estimate of Kodolányi et al. (2022) calculated from CC and NC troilite compositions. The displayed initial ^{60}Fe/^{56}Fe estimates of Tang & Dauphas (2015) and Kodolányi et al. (2022) overlap. (b) The same as (a) but with an additional data point in each panel (colored and black symbols), which correspond to the average ^{60}Fe/^{56}Fe ratios of the given isotope reservoir at the formation of CCAIs (^{60}Fe/^{56}Fe$_{CCAI}$ ratios). These ratios were calculated from the results of regressions [5], using the average age of chondrules in the given isotope reservoir. The average age for the right panel was calculated by mixing the weighted average ^{26}Al/^{27}Al ratios calculated for CC and NC chondrules (see Section 5.6) in a 56:30 ratio (i.e., in the ratio of our nickel isotope data in Table 5 after the removal of the anomalous ^{60}Ni/^{62}Ni ratios discussed in Section 5.3), and using this average to derive an average age relative to CCAI formation (2.10 ± 0.01 Myr).

^{56}Fe/^{62}Ni ratios are higher than those from chondrule b4 of MET 00426 (Table 5; Figure 6(a), (b)). The two anomalous ^{60}Ni/^{62}Ni ratios of NWA 8276 have, however, large uncertainties (3%–4%). Importantly, it is because of these two anomalous results that the inferred initial ^{60}Fe/^{56}Fe ratio of chondrule b15 from NWA 8276 is negative (-1.01 (± 0.43) $\times$ 10^{-6}). The ^{60}Ni/^{62}Ni ratios from these two measurements do not only differ from the terrestrial ^{60}Ni/^{62}Ni ratio by more than 2σ, but also from the weighted average of all our nickel isotope data omitting the three anomalous ^{60}Ni/^{62}Ni ratios from MET 00426 (7.206 ± 0.012; $n = 88$, MSWD = 0.91). Assuming no effect of in situ iron-60 decay on present-day nickel-60 abundance, two anomalously subterrestrial ^{60}Ni/^{62}Ni ratios could be consistent with stochastic variations around the average, terrestrial, value. However, to measure both such anomalous compositions in the same chondrule, as is the case for the two anomalous ^{60}Ni/^{62}Ni ratios from NWA 8276, is unlikely. Apart from mass-dependent isotope fractionation, such a distribution of results could also be caused by some kind of analytical bias, e.g., interference on mass 62. Nevertheless, although *some* kind of bias cannot be ruled out, an oxide interference on mass 62 can. Analyses from NWA 8276 chondrule b20 have higher (^{46}Ca + ^{46}Ti)/^{62}Ni ratios than those measured in the same week on the two spots with anomalous ^{60}Ni/^{62}Ni ratios in the same sample's chondrule b15, yet they show terrestrial or higher ^{60}Ni/^{62}Ni ratios (Table 5). This is opposite to what is expected in the case of a ^{46}Ca^{16}O + ^{46}Ti^{16}O interference. Regardless of the cause of the anomalous ^{60}Ni/^{62}Ni ratios in chondrule b15 however, similar to the anomalous data from MET 00426, these anomalous compositions probably do not represent stochastic variations (only). Therefore, we repeated the weighted linear regression of our UOC data without the anomalous data of NWA 8276. The calculated initial ^{60}Fe/^{56}Fe is $9.8(\pm 9.9) \times 10^{-8}$ ($n = 56$, MSWD = 0.81; regression [2] in the center panel of Figure 7(a)), higher than the ratio calculated for the data set with the anomalous points of NWA 8276.

Naturally, mass-dependent isotope fractionation could have affected more of the studied chondrules. Since our data are not-normalized internally, we could only detect such shifts in

isotope composition if they were large enough to cause data to appear outside the range expected from the uncertainties of our measurements. However, as long as no such outliers occur, the effect of fractionated compositions remains insignificant for the calculation of average initial $^{60}Fe/^{56}Fe$ ratios because it will be indistinguishable from the normal measured compositional variation.

5.4. Correlated Uncertainties of Isotope Ratios

Given the facts that the denominator isotope of the two sets of isotope ratios used for weighted linear regression is the same (nickel-62), and some of the measurements have low nickel count rates ($^{62}Ni < 1$ count per second; Table 2), our linear regression results may be influenced by correlated uncertainties of $^{60}Ni/^{62}Ni$ and $^{54}Fe/^{62}Ni$ ratios (remember, our reported $^{56}Fe/^{62}Ni$ ratios were calculated from measured $^{54}Fe/^{62}Ni$ ratios). If ignored, correlated uncertainties can lead to an erroneous slope of the regression line. We estimated the correlation between uncertainties using Monte Carlo simulations (Thomas Stephan, private communication), based on the total amount of counts on each measured isotope and the uncertainties of isotopic and elemental fractionation factors. Average initial $^{60}Fe/^{56}Fe$ ratios calculated from linear regressions that take into account the correlation between the uncertainties of $^{54}Fe/^{62}Ni$ and $^{60}Ni/^{62}Ni$ ratios (regressions [4] and [5] in Figure 7) match closely the respective $^{60}Fe/^{56}Fe$ ratios calculated without considering the correlation of uncertainties (regressions [1] and [2]) for our CC chondrule data and the entire data set (left and right panels, respectively, in Figure 7), with the differences being only a few percent. However, for our UOC data, $^{60}Fe/^{56}Fe$ ratios calculated with consideration of correlated uncertainties are 15%–42% lower than the corresponding $^{60}Fe/^{56}Fe$ ratios calculated neglecting the correlation of uncertainties (center panels of Figure 7).

5.5. Average $^{60}Fe/^{56}Fe$ Ratios of the Studied Chondrules

Based on the presence of mass-dependent isotope fractionation effects, and the correlation between the uncertainties of $^{56}Fe/^{62}Ni$ and $^{60}Ni/^{62}Ni$ ratios, the most realistic estimation of the average initial $^{60}Fe/^{56}Fe$ ratio of our chondrules should omit the anomalous $^{60}Ni/^{62}Ni$ ratios of chondrules b4 and b15 of MET 00426 and NWA 8276, respectively, but include the correlation of uncertainties. For our CC samples, the average initial $^{60}Fe/^{56}Fe$ ratio estimated from such a regression is 2.1 (± 1.3) $\times 10^{-7}$ ($n = 30$, MSWD = 0.83; regression [5] in the left panels of Figure 7), which overlaps with the estimate of Steele et al. (2012) for bulk IVB iron meteorites (same isotope reservoir), 0.75 (± 0.33) $\times 10^{-7}$ (horizontal thin black lines with yellow $\pm 1\sigma$ uncertainty band in Figure 7(a), (b)). For our UOC chondrules (NC isotope reservoir), the same procedure yields an average initial $^{60}Fe/^{56}Fe$ ratio of 0.84 (± 0.99) $\times 10^{-7}$ ($n = 56$, MSWD = 0.83; regression [5] in the center panels of Figure 7), which is nominally lower, but, within uncertainty, identical to the initial $^{60}Fe/^{56}Fe$ ratio estimated for our CC chondrules (the difference being 1.3 (± 1.6) $\times 10^{-7}$). Given the associated uncertainty, our UOC estimate is also identical to the initial $^{60}Fe/^{56}Fe_{CCAI}$ ratio estimated by Tang & Dauphas (2015) based on bulk quenched angrites, eucrites, and UOC chondrules (1.01 (± 0.14) $\times 10^{-8}$; horizontal thick blue line in Figure 7(a)) as well as the initial $^{60}Fe/^{56}Fe$ ratio we estimated earlier for chondritic troilites (1.1 (± 1.5) $\times 10^{-8}$; Kodolányi et al. 2022 horizontal gray bands in Figure 7(a), (b)). The overlap with the Tang & Dauphas (2015) estimate is consistent with the fact that these authors used data predominantly from meteorites that belong to the NC isotope reservoir for their calculation. If we combine our CC and NC data, we obtain $^{60}Fe/^{56}Fe = 0.97$ (± 0.71) $\times 10^{-7}$ (MSWD = 0.83).

5.6. Average $^{60}Fe/^{56}Fe$ Ratio of the Solar System at Formation

As shown in the previous section, the difference between estimated initial $^{60}Fe/^{56}Fe$ ratios of different isotope reservoirs is $<2\sigma$, i.e., statistically not significant at the precision of our analysis. Nevertheless, CC chondrules have nominally higher inferred $^{60}Fe/^{56}Fe$ ratios than NC chondrules (Figure 7(a)). Assuming the observed difference is real, and the solar system had a uniform $^{60}Fe/^{56}Fe_{CCAI}$ ratio (as assumed by previous studies), this is surprising because CC chondrules are in general slightly younger than NC chondrules (see below). Furthermore, our limited aluminum–magnesium isotope measurements do not indicate that the NC chondrules studied here are for some reason younger, on average, than similar chondrules studied before (see Section 5.2).

To evaluate the consequence of the age difference between CC and NC chondrules quantitatively, we calculated $^{60}Fe/^{56}Fe_{CCAI}$ ratios from data of the two sets of chondrules, using the average initial $^{60}Fe/^{56}Fe$ ratios discussed above (regression [5]), and available chondrule age data. For the calculation of average ages, we used the weighted averages of initial $^{26}Al/^{27}Al$ ratios reported in the literature for CC (CO and CM chondrites plus Acfer 094) and NC (UOC) chondrules (Rudraswami & Goswami 2007; Kurahashi et al. 2008; Villeneuve et al. 2009; Ushikubo et al. 2013; Hertwig et al. 2019; Pape et al. 2019; Siron et al. 2021; Fukuda et al. 2022). The calculated average age of CC chondrules (2.37 ± 0.01 Myr after CCAIs) is ~0.4 Myr younger than that of NC chondrules (1.98 ± 0.01 Myr after CCAIs). The nominal difference between the average $^{60}Fe/^{56}Fe_{CCAI}$ ratios calculated using the CC and NC chondrule data sets is thus bigger than the difference between the initial $^{60}Fe/^{56}Fe$ ratios of the same chondrule populations, but statistically still not significant, because of the large uncertainties: the $^{60}Fe/^{56}Fe_{CCAI}$ ratio calculated from CC chondrule data is 4.0 (± 2.4) $\times 10^{-7}$, whereas that calculated from NC chondrule data is 1.4 (± 1.7) $\times 10^{-7}$ (Figure 7(b)). For our combined data set we obtain $^{60}Fe/^{56}Fe_{CCAI} = 1.8$ (± 1.3) $\times 10^{-7}$ (see explanation in the legend of Figure 7(b)).

Whether or not age adjusted, the inferred average $^{60}Fe/^{56}Fe$ ratios of the studied chondrules are higher than those suggested by most previous bulk analyses and our previously published in situ troilite data. However, the large uncertainties render the "high" average $^{60}Fe/^{56}Fe$ ratios calculated for our chondrules less significant (Figure 7(a), (b)). The difference between the average $^{60}Fe/^{56}Fe_{CCAI}$ ratio derived from our CC chondrule data and the estimate given by Steele et al. (2012) based on the composition of IVB iron meteorites, which are from the same isotope reservoir, is just slightly more than 1σ (difference: 3.2 (± 2.5) $\times 10^{-7}$). The differences between the average $^{60}Fe/^{56}Fe_{CCAI}$ ratio calculated from our CC chondrule data and the $^{60}Fe/^{56}Fe_{CCAI}$ ratios estimated by Cook et al. (2021) for the (isotopically also CC) IVB and IID meteorite precursors (5.8 (± 1.2) $\times 10^{-7}$ and 7.9 (± 1.9) $\times 10^{-7}$, respectively) are statistically also not significant (-1.8 (± 2.7) $\times 10^{-7}$ and -3.9 (± 3.1) $\times 10^{-7}$, respectively), especially if we consider the

additional uncertainty of the Cook et al. (2021) estimates, that stems from the choice of reference $^{60}Ni/^{58}Ni$ ratio (see Introduction). Similarly, the $^{60}Fe/^{56}Fe_{CCAI}$ ratio calculated from our NC chondrules is identical within uncertainty with the 1.01 $(\pm 0.14) \times 10^{-8}$ value estimated by Tang & Dauphas (2015) based on bulk NC meteorite samples.

5.7. Comparison with Previous In Situ Silicate Data

Past in situ measurements of many individual chondrules using SIMS or NanoSIMS indicated initial $^{60}Fe/^{56}Fe$ ratios well in excess of 10^{-7} (e.g., Mishra & Chaussidon 2014; Mishra et al. 2016; Telus et al. 2018), with the maximum value exceeding 10^{-6} (Mishra & Goswami 2014). Based on the reported uncertainties, the high inferred $^{60}Fe/^{56}Fe$ ratios are, in most cases, well resolved from the initial $^{60}Fe/^{56}Fe$ ratios inferred from the isotope composition of bulk samples, which has been the central problem in the discussion around early solar system iron-60 abundance (see Section 1). Three such high $^{60}Fe/^{56}Fe$ ratios are displayed in Figure 6 (lines 1–3). Given the large amount of available in situ isotope data, it is imperative to analyze our results in the context of previous measurements.

Nevertheless, the task is not trivial. Our data do not allow precise isochrons to be determined for individual chondrules (see Section 4.4). Therefore, to compare our results with data from previous SIMS and NanoSIMS measurements (Mishra & Goswami 2014; Mishra & Chaussidon 2014; Mishra et al. 2016; Telus et al. 2018), we must combine the data of each study, similar to how we combined our own isotope data, to obtain average initial $^{60}Fe/^{56}Fe$ ratios.

We should mention here that all but one study from the above list used internal normalization to the $^{61}Ni/^{62}Ni$ ratio to correct for instrumental and cosmogenic mass fractionation effects, so for a fair comparison, we used the internally not-normalized isotope data from each study. As noted in Section 5.3, the effect of instrumental mass fractionation is negligible on our data (and, based on the similarity of the analytical techniques, we believe it to be negligible on literature data as well), and for the comparison, we removed those data from our set that we suspected to reflect mass-dependent isotope fractionation resulting from early solar system processes (see Section 5.3). Reported $^{56}Fe/^{61}Ni$ ratios (e.g., Mishra & Chaussidon 2014) were recalculated to obtain $^{56}Fe/^{62}Ni$ ratios, using $^{62}Ni/^{61}Ni$ ratios that could be calculated from reported isotope anomalies. We did not correct for the effect of correlated uncertainties during linear regression, because correlation coefficients were only available for the data of Telus et (2018, note that these authors did not include the effect of isotopic and element fractionation factors in the calculation of correlation coefficients). As shown above however (Section 5.4), correlated uncertainties may have a non-negligible effect on calculated initial $^{60}Fe/^{56}Fe$ ratios, so the fact that correlated uncertainties were disregarded may be the biggest caveat of our comparison. Whether the literature data are comparable with each other is also a concern. For example, Mishra & Goswami (2014) as well as Mishra & Chaussidon (2014) used measurements on mass 56.5 to estimate the dynamic background for all analyzed isotopes, whereas Mishra et al. (2016) used mass 57.5 for the same purpose. In contrast, Telus et al. (2018) did not measure the dynamic background. The approach shared by the first three of these studies has an inherent risk because it is based on the assumption that the dynamic background is mass-independent. Correction of the dynamic background using a single intensity value will lead to an increase in any isotope ratio in which the more abundant isotope is the numerator, such as the $^{60}Ni/^{62}Ni$ or $^{62}Ni/^{61}Ni$ ratios. Depending on the signal-to-background ratio, this effect can be enormous. To remain with the example of Mishra & Goswami (2014), using their quoted intensity data and the intensity plots in the Electronic Appendix of their paper, the above "single-value-background-correction approach" introduced an about 4 per mil increase in the $^{60}Ni/^{62}Ni$ ratio for an object with a $^{56}Fe/^{62}Ni$ ratio of about 220,000, relative to the same object's uncorrected $^{60}Ni/^{62}Ni$ ratio. This is more than a third of the maximum positive anomaly these authors observed in measured $^{60}Ni/^{62}Ni$ ratios in their data set at about the same $^{56}Fe/^{62}Ni$ ratio when compared to the terrestrial $^{60}Ni/^{62}Ni$ ratio ($\sim$11 ‰). To put it another way, even in a chondrule with terrestrial nickel isotope composition, Mishra & Goswami (2014) could have calculated an initial $^{60}Fe/^{56}Fe$ ratio up to the order of $\sim 10^{-7}$, depending on the validity of the assumption of constant dynamic background. We tried to verify this assumption using our NanoSIMS (note that from the above studies only that of Mishra et al. 2016 used the same instrument as we did). First, we measured the dynamic background of ^{62}Ni in our terrestrial enstatite standard ($Fe/Ni = 459 \pm 89$, $FeO = 17.54 \pm 0.10$ wt.%), as we would do for one of our chondrule measurements (see Section 3.2.2), then used the same detector to measure the dynamic background on mass 57.5, as done by Mishra et al. (2016). For the latter measurement, we assumed that "57.5" refers to the mass exactly halfway between the peaks of ^{57}Fe and $^{58}Fe + {}^{58}Ni$ (the latter two isotopes cannot be resolved with the NanoSIMS spectrometer). The dynamic background intensities measured were 0.004 ± 0.002 and $0.064+0.007/-0.006$ counts per second, respectively. This suggests that the dynamic background is mass-dependent, at least for isotopes with orders of magnitude abundance contrast. The above train of thoughts is not intended to question the results of any of the above authors (again, background correction becomes critical at low signal-to-background ratios only), but to highlight the potential effect of background correction, and to urge the reader to keep this effect in mind when comparing literature data sets with each other and the results of the present study.

With the above caveats in mind, let us now examine how the new and old data compare. The average initial $^{60}Fe/^{56}Fe$ ratio of the combined isotope data from the literature is 1.0 $(\pm 2.8) \times 10^{-7}$ for CC (CV) chondrules ($n = 47$, MSWD = 0.75) and -1.13 $(\pm 0.30) \times 10^{-8}$ for NC (UOC) chondrules ($n = 551$, MSWD = 5.29). Although given the uncertainties, the average $^{60}Fe/^{56}Fe$ ratio calculated for CC chondrules matches the ratio we calculated from our CC isotope data (2.1 $(\pm 1.3) \times 10^{-7}$; regression [2] in the left panel of Figure 7(a)), the negative average initial $^{60}Fe/^{56}Fe$ ratio calculated for NC chondrules does not. The negative slope of the regression line of NC chondrules from the literature is entirely due to the Telus et al. (2018) data set. Performing the same linear regression on the Telus et al. (2018) data set only gives an average initial $^{60}Fe/^{56}Fe$ ratio of -1.36 $(\pm 0.31) \times 10^{-8}$ ($n = 350$, MSWD = 6.95), whereas the average initial $^{60}Fe/^{56}Fe$ ratio that can be calculated from the NC chondrule data of the other three studies is 1.21 $(\pm 0.21) \times 10^{-7}$ ($n = 201$, MSWD = 1.83), identical to the initial $^{60}Fe/^{56}Fe$ ratio calculated from our NC data (minus the anomalous $^{60}Ni/^{62}Ni$ ratios from NWA 8276):

9.8 ($\pm$9.9) $\times$ 10^{-8} (regression [2] in the middle panel of Figure 7(a)). Interestingly, if we redo the linear regression on the Telus et al. (2018) data set but this time exclude data with ^{56}Fe/^{62}Ni ratios above 330,000 (i.e., the limit above which the number of measurement points in our as well as literature data drastically decreases; Figure 6), the inferred average ^{60}Fe/^{56}Fe ratio becomes positive, but still not in line with the average initial ^{60}Fe/^{56}Fe ratio calculated from the data of the remaining three studies: 2.10 ($\pm$0.72) $\times$ 10^{-8} ($n = 290$, MSWD = 7.35). Nevertheless, the relatively high MSWD values calculated for the ^{60}Fe/^{56}Fe ratio estimates based on the Telus et al. (2018) data (6.95 and 7.35) indicate that there are variations in their data set beyond what is expected based on the measurement uncertainties, which remain, regardless of whether the regression is performed on the entire data set, or on the nickel-rich data only. This makes a direct comparison of the Telus et al. (2018) data with ours and the rest of the literature data more difficult.

Based on the above comparisons and the considerations regarding data compatibility, the results of the current study are consistent with the SIMS and NanoSIMS data reported earlier, if the literature data are treated as a whole, but the consistency is rendered less meaningful by the large uncertainties of our data and the fact that literature data do not compare well. This highlights the disadvantage of using SIMS or NanoSIMS isotope data for the estimation of initial ^{60}Fe/^{56}Fe ratios: these techniques, although capable of delivering high-quality data, are challenged by the small isotope anomalies expected, and by the poor counting statistics resulting from their limited sensitivity (relative to, e.g., resonance ionization mass spectrometry).

6. Summary and Conclusions

We report new in situ isotope analyses by NanoSIMS on 14 silicate chondrules from six petrologic type $\sim$3 CC and NC meteorites. The new iron-nickel isotope data were obtained using a special NanoSIMS setup for increased spatial control (200–300 nm), which helped to reduce the potential bias introduced by the inclusion of unwanted phases. NanoSIMS was also used for aluminum–magnesium isotope measurements to estimate the age of some chondrules. Isotope analyses were complemented by SEM-EDX and EPMA measurements of major chondrule phases, as well as by the TEM study of three of the chondrules. The combination of isotope data with micro and nanoscale petrography and major and minor element compositions allows us to further constrain the initial ^{60}Fe/^{56}Fe ratio of the solar system and to give directions for follow-up research.

Without data likely influenced by mass-dependent isotope fractionation, and considering the effects of correlated uncertainties of ^{56}Fe/^{62}Ni and ^{60}Ni/^{62}Ni ratios, our best estimate of the average initial ^{60}Fe/^{56}Fe ratio of the studied CC chondrules is 2.1 ($\pm$1.3) $\times$ 10^{-7}. This is identical within uncertainty with the ^{60}Fe/^{56}Fe ratio inferred for IVB iron meteorites, a group that also belongs to the CC meteorites (0.75 ($\pm$0.33) $\times$ 10^{-7}; Steele et al. 2012), and only slightly more than 1σ off the same value if adjusted for the average age of CC chondrules (4.0 ($\pm$2.4) $\times$ 10^{-7}). The average estimated initial ^{60}Fe/^{56}Fe ratio of the studied NC chondrules is 0.8 ($\pm$1.0) $\times$ 10^{-7}. Regardless of whether we consider the average age of NC chondrules or not, this is again consistent with the ^{60}Fe/^{56}Fe ratio estimated for the same isotope reservoir at solar system birth based on previous isotope data from bulk meteorites and chondrules (1.01 ($\pm$0.14) $\times$ 10^{-8}; Tang & Dauphas 2015).

Our silicate isotope data are thus consistent with the low initial ^{60}Fe/^{56}Fe ratios inferred from isotope measurements of bulk meteorites, and our previously published in situ data on chondritic troilites (1.0 ($\pm$1.5) $\times$ 10^{-8}; Kodolányi et al. 2022), but inconsistent with ^{60}Fe/^{56}Fe ratios $>2.4 \times 10^{-7}$ (2σ upper limit of our entire data set) reported in the literature for some chondrule silicates based on in situ isotope data (e.g., Mishra & Goswami 2014). A more detailed comparison of our results with in situ data from the literature is difficult however, despite the fact that most of the in situ literature data were collected using SIMS or NanoSIMS because of differences in analytical procedures (e.g., measurement and correction of dynamic background) and the calculation of initial ^{60}Fe/^{56}Fe ratios (consideration of correlated uncertainties).

Our data may support the idea that the average initial ^{60}Fe/^{56}Fe ratio of the CC isotope reservoir was higher than that of the NC isotope reservoir, although the difference that can be calculated from our data set is statistically not significant. Nonetheless, this point deserves further attention, and could be best addressed by further in situ measurements of primitive chondrites using the more precise and less bias-prone resonant ionization mass spectrometry technique, or by the bulk analysis of differentiated meteorites from the CC isotope reservoir that span a large range of Fe/Ni ratios.

We thank Elmar Gröner and Philipp Schuhmann for technical support on NanoSIMS and Thomas Stephan for his help with linear regression calculations. Our project was financially supported by the German Research Foundation (DFG) Special Priority Program 1833 (grant Nos.: HO2163/3-1, VO1816/4-1). Thin sections of QUE 97008, MET 00526, MET 00426, ALHA77307, and DOM 08006 were provided by the Antarctic Search for Meteorites (ANSMET) program. US Antarctic meteorite samples are recovered by the ANSMET program which has been funded by NSF and NASA, and characterized and curated by the Department of Mineral Sciences of the Smithsonian Institution and Astromaterials Curation Office at NASA Johnson Space Center. We thank Knut Metzler (WWU) for lending a thin section of NWA 8276. We also acknowledge funding of the ThermoFisher TEM "Themis" by the DFG via the Major Research Instrumentation Program under INST 211/719-1. Helpful comments of an anonymous reviewer are very much appreciated.

Appendix

Supplementary Figure A1.

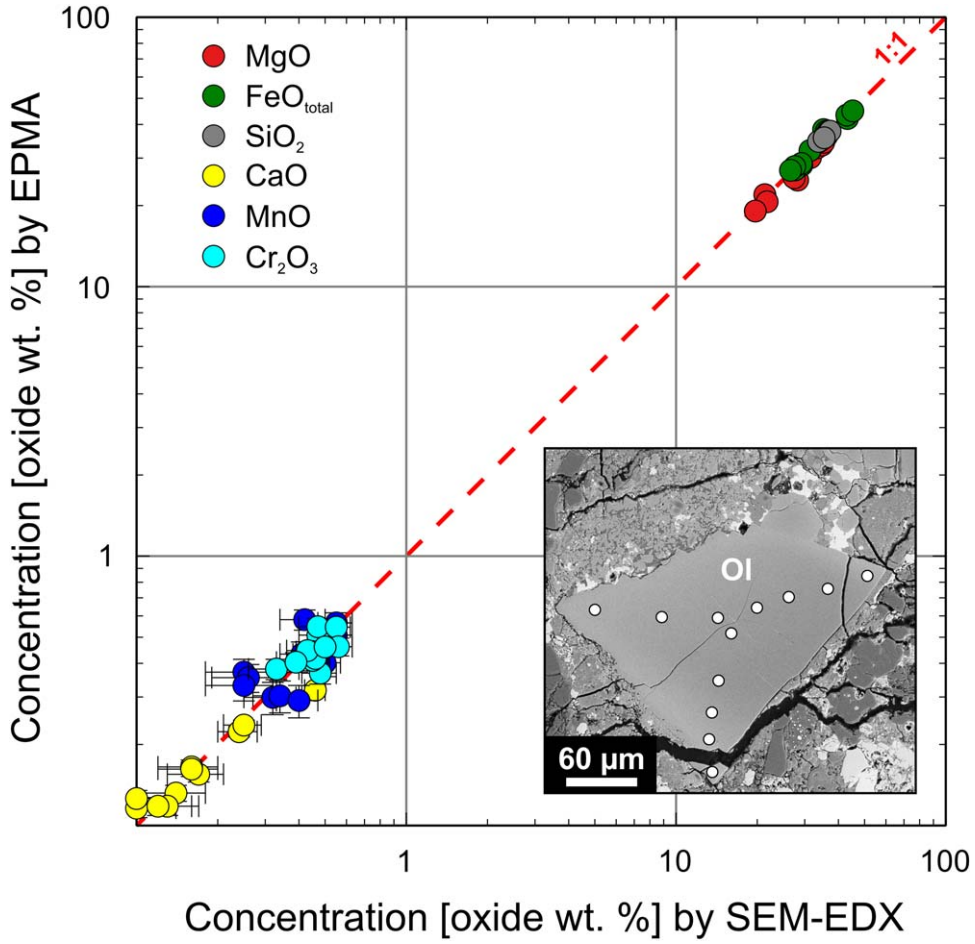

Figure A1. Comparison of EDX and EPMA data (with 1σ measurement uncertainties) in an olivine from DOM 08006 (BSE image; white dots represent the analysis spots). Ol = olivine. FeO_{total} = all iron reported as FeO.

ORCID iDs

János Kodolányi https://orcid.org/0000-0001-5710-0537
Peter Hoppe https://orcid.org/0000-0003-3681-050X
Christian Vollmer https://orcid.org/0000-0002-7768-7651

References

Armstrong, J. T. 1991, in Electron Probe Quantitation, ed. K. F. J. Heinrich & D. E. Newbury (Boston, MA: Springer), 261
Castillo-Rogez, J., Johnson, T. V., Lee, M. H., et al. 2009, Icar, 204, 658
Cook, D. L., Meyer, B. S., & Schönbächler, M. 2021, ApJ, 917, 59
De Hoog, J. C. M., Gall, L., & Cornell, D. H. 2010, ChGeo, 270, 196
Fukuda, K., Tenner, T. J., Kimura, M., et al. 2022, GeCoA, 322, 194
Gramlich, J. W., Machlan, L. A., Barnes, I. L., & Paulsen, P. J. 1989, J. Res. Natl. Inst. Stand. Technol., 94, 347
Hertwig, A. T., Makoto, K., Ushikubo, T., Defouilloy, C., & Kita, N. T. 2019, GeCoA, 253, 111
Hoppe, P., Cohen, S., & Meibom, A. 2013, Geostand. Geoanal. Res., 37, 111
Hublet, G., Debaile, V., Wimpenny, J., & Yin, Q.-Z. 2017, GeCoA, 218, 73
Jacobsen, B., Yin, Q., Moynier, F., et al. 2008, E&PSL, 272, 353
Kodolányi, J., Hoppe, P., Vollmer, C., Berndt, J., & Müller, M. 2022, ApJ, 929, 107
Kruijer, T., Burkhardt, C., Budde, G., & Kleine, T. 2017, PNAS, 114, 6712
Kurahashi, E., Kita, N. T., Nagahara, H., & Morishita, Y. 2008, GeCoA, 72, 3865
Larsen, K. K., Trinquier, A., Paton, C., et al. 2011, ApJL, 735, L37
Lauretta, D. S., Nagahara, H., & Alexander, C. M. 2006, in Meteorites and the Early Solar System II, ed. D. S. Lauretta & H. Y. McSween (Tucson, AZ: Univ. Arizona Press), 431
Liszewska, K. M., Rundhaug, C. J., Hunt, A. C., & Schönbächler, M. 2021, in 84th Annual Meeting of the Meteoritical Society (Chantilly, VA: Meteoritical Society), 6175
Mahon, K. I. 1996, IGRv, 38, 293
McKibbin, S. J., Ireland, T. R., Amelin, Y., & Holden, P. 2015, GeCoA, 157, 13
Mishra, R. K., & Chaussidon, M. 2014, E&PSL, 398, 90
Mishra, R. K., & Goswami, J. N. 2014, GeCoA, 132, 440
Mishra, R. K., Marhas, K. K., & Sameer 2016, E&PSL, 436, 71
Moskovitz, N., & Gaidos, E. 2011, M&PS, 46, 903
Mostefaoui, S., Lugmair, G. W., & Hoppe, P. 2005, ApJ, 625, 271
Nanne, J. A. M., Nimmo, F., Cuzzi, J. N., & Kleine, T. 2019, E&PSL, 511, 44
Neumann, W., Kruijer, T. S., Breuer, D., & Kleine, T. 2018, JGRE, 123, 421
Norris, T. L., Gancarz, A. J., Rokop, D. J., & Thomas, K. W. 1983, JGR, 88, B331
Pape, J., Mezger, K., Bouvier, A.-S., & Baumgartner, L. P. 2019, GeCoA, 244, 416
Rudraswami, N. G., & Goswami, J. N. 2007, E&PSL, 257, 231
Rugel, G., Faestermann, T., Knie, K., et al. 2009, PhRvL, 103, 072502
Schiller, M., Baker, J. A., & Bizzarro, M. 2010, GeCoA, 74, 4844
Siron, G., Fukuda, K., Kimura, M., & Kita, N. T. 2021, GeCoA, 293, 103
Slodzian, G., Hillion, F., Stadermann, F. J., & Zinner, E. 2004, ApSS, 231-232, 874
Spitzer, F., Burkhardt, C., Nimmo, F., & Kleine, T. 2021, E&PSL, 576, 117211
Steele, R. C. J., Coath, C. D., Regelous, M., Russell, S., & Elliott, T. 2012, ApJ, 758, 59
Steele, R. C. J., Elliott, T., Coath, C. D., & Regelous, M. 2011, GeCoA, 75, 7906
Tang, H., & Dauphas, N. 2012, E&PSL, 359, 248
Tang, H., & Dauphas, N. 2015, ApJ, 802, 22
Telus, M., Huss, G. R., Nagashima, K., Ogliore, R. C., & Tachibana, S. 2018, GeCoA, 221, 342
Telus, M., Huss, G. R., Ogliore, R. C., et al. 2016, GeCoA, 178, 87
Trappitsch, R., Boehnke, P., Stephan, T., et al. 2018, ApJ, 857, L15
Ushikubo, T., Nakashima, D., Kimura, M., Tenner, T. J., & Kita, N. T. 2013, GeCoA, 109, 280
Villeneuve, J., Chaussidon, M., & Libourel, G. 2009, Sci, 325, 985
Warren, P. H. 2011, E&PSL, 311, 93